Advances in Nano Research, *Vol. 18, No. 1 (2025) 33-52*
https://doi.org/10.12989/anr.2025.18.1.033

Size dependent dynamics of a bi-directional functionally graded nanobeam via machine learning methods

Aiman Tariq*, Büşra Uzun[a], Murat Akpınar[b], Mustafa Özgür Yaylı[c] and Babür Deliktaş[d]

Department of Civil Engineering, Artificial Intelligence and Computational Mechanics Laboratory, Bursa Uludag University, Görükle Campus, 16059, Bursa/Turkey

(*Received September 12, 2024, Revised December 26, 2024, Accepted January 2, 2025*)

Abstract. This study explores the lateral vibration behavior of bi-directional functionally graded nanobeams using a combination of semi-analytical and machine learning approaches. The semi-analytical method uses the Fourier sine series and Stokes' transform for the deflection function of a bi-directional functionally graded nanobeam constrained by elastic springs at both ends and considers nonlocal modified couple stress theory to account for size effects. In the last step of the method, an eigenvalue problem is derived and the resulting frequency values are then used to train machine learning models, including extreme gradient boosting (XGB), artificial neural networks (ANN) and decision tree regression (DTR). The models' ability to predict the nanobeam's natural frequencies is evaluated using metrics like R^2, MAE, MAPE, RMSE, and the A20-index, alongside visual tools such as scatter plots, radar plots, and Taylor diagrams. The results indicate that ML models can accurately predict the natural frequencies of a bi-directional functionally graded nanobeams when provided with sufficient training data. In particular, ANN demonstrated exceptional generalization capability by achieving the highest R^2 and the lowest MAE, MAPE, and RMSE on both the training and testing datasets. The impact of various effects on vibration frequencies is detailed through a series of graphs and tables.

Keywords: artificial neural network; bi-directional functionally graded nanobeam; machine learning; nonlocal modified couple stress theory; size effect

1. Introduction

Nowadays, in the field of nanotechnology, composite materials have been the subject of numerous studies due to their variable and unique structure. These materials exhibit different mechanical, thermal, and electrical properties, providing unprecedented benefit to various engineering applications. In this context, composites have increased their potential applications by providing new opportunities for researchers to develop next-generation nanoscale devices and multifunctional materials. Some of the fields where composites are used are sensors (Hasan *et al*. 2021, Müller *et al*. 2003), electronics and optoelectronics (Aziz *et al*. 2017, Zyoud *et al*. 2023), medicine (Heidary *et al*. 2023, Watari *et al*. 2004), construction materials (Akshaya *et al*. 2021), energy absorption systems (Cui *et al*. 2009), and RF capacitor systems (Rao *et al*. 2001, Rao and Wong 2004).

Currently, researchers have focused their studies on functionally graded materials (FGMs), which are known as an advanced type of composite materials. FGMs, which were first developed in 1984 for a Japanese spaceplane project (Bohidar *et al*. 2014), have been able to solve the problems of traditional composite materials, such as delamination and low heat resistance.

Considering the wide range of applications of composite materials and their evolving structural complexity, it has become essential to perform both dynamic and static analyses of these materials, especially at the nanoscale. Understanding and predicting the behavior of composites is essential not only to optimize their performance, but also to advance the design and implementation of next-generation nanoscale devices and systems. In literature, classical theories (CTs) have been derived to study the static and dynamic behavior of composite materials. However, CTs do not yield results consistent with experiments performed at nanoscale and new formulations need to be derived. In this context, various theories have been proposed for the dynamic analysis of nanostructures that include a material length scale parameter in their formulations. One of these methods, the nonlocal elasticity theory (NT), was presented by Eringen (1977). Using the NT, Uymaz (2013) performed forced vibration analysis of functionally graded (FG) nanobeams whose material characteristics change through the thickness. In a different paper, Zargaripoor *et al*. (2018) investigated the free vibration of FG nanoplates utilizing NT. Also in that study, the finite element method (FEM) was applied to model the FG nanoplate. Li and Hu (2017) presented the torsional vibration of FG tubes with changing material characteristics along the radial and axial directions on the basis of NT. Nejad *et al*. (2016) conducted studies on the buckling response of bi-directional functionally graded nanobeam (BD-FGNB) with the help of NT. Hosseini and

*Corresponding author, Ph.D.,
E-mail: aimantariq@uludag.edu.tr
[a] Assistant Professor, E-mail: buzun@uludag.edu.tr
[c] M.Sc. Student, E-mail: muratakpinar@uludag.edu.tr
[d] Professor., E-mail: ozguryayli@uludag.edu.tr
[e] Professor., E-mail: bdeliktas@uludag.edu.tr

ISSN: 2287-237X (Print), 2287-2388 (Online)

Rahmani (2016) studied the thermal buckling and dynamic behavior of a curved FG nanobeam whose material properties change in the radial direction based on NT. Hosseini-Hashemi *et al*. (2013) examined the free vibration analysis of thick, circular, and FG Mindlin nano-sized plates with different boundary conditions using NT. In addition to the studies using NT (Hao-nan *et al*. 2021, Jung and Han 2013, Lal and Dangi 2019, Pirmoradian *et al*. 2020), strain gradient theory (SGT) is also frequently preferred in the literature.

SGT, has been established by Fleck and Hutchinson (1993, 1997, 2001). Ansari *et al*. (2013) studied the buckling, bending, and free vibration behavior of FG Timoshenko nanobeams by means of SGT. Employing SGT in the equations, Rahaeifard *et al*. (2013) studied the size-dependent dynamic and static behavior of FG nonlinear beams where the material properties vary along the thickness of the beam based on a power law of the volume fraction. Pham *et al*. (2022) examined the dynamic instability of magnetically embedded FG porous nanobeams by the finite element modeling, combining SGT and the higher-order shear deformation beam theory. In addition to studies with SGT (Nguyen *et al*. 2019, Shishesaz *et al*. 2017), there are also studies in the literature using the nonlocal strain gradient theory (NSGT) proposed by Lam *et al*. (2003). Using the aforementioned NSGT, Li *et al*. (2017) investigated the dynamic behavior of a two-component axial FG size-dependent inhomogeneous beam model. Gao *et al*. (2019) investigated the nonlinear free vibration of FG nanotubes using the high-order shear deformation beam theory (SDBT) and NSGT. Al-Shujairi and Mollamahmutoğlu (2018) analyzed the dynamic behavior of FG sandwich microbeam subjected to parametric axial excitation with various support conditions on the basis of first-order SDBT and NSGT. Besides the articles using NSGT (Civalek *et al*. 2023, Esen *et al*. 2021, Li *et al*. 2021, Shen *et al*. 2020), modified strain gradient theory (MSGT) is also one of the methods preferred by researchers. For instance, Akgöz and Civalek (2013) carried out studies on the size-dependent buckling response of FG micro-sized beams for different boundary conditions utilizing MSGT. Karamanli and Vo (2020) performed stability, static and free dynamic analyses of FG micro-sized beams using MSGT, modeling the variation of material properties along the thickness with Mori-Tanaka homogenization scheme. Karamanli and Vo (2021) investigated the size-dependent mechanical behavior of FG porous microbeams using MSGT and quasi-3D theory. Thai *et al*. (2017) studied the static and dynamic responses of FG microplates in the context of isogeometric analysis and MSGT.

The concept of couple-stress in materials was first proposed by Voigt (1887). However, Cosserat and Cosserat (1909) developed the first mathematical model to analyze couple-stresses. Later, couple stress theory (CST) was introduced by Toupin (1962), Mindlin and Tiersten (1962), and Koiter (1969). In subsequent studies, Yang *et al*. (2002) added a material size parameter to the formulations and proposed the modified couple stress theory (MCST). Şimşek and Reddy (2013a), who used MCST in their study, performed free vibration and static bending analyses of FG microbeams. In another work, Şimşek and Reddy (2013b) studied the buckling of a FG microbeam embedded in elastic Pasternak media by applying MCST theory. Ghadiri and Shafiei (2016) investigated the thermal vibration of a rotating FG Timoshenko microbeam exposed to four distinct types of thermal loading using MCST. Ke and Wang (2011) investigated the dynamic analysis of FG microbeams where the material characteristics vary in the height direction based on Timoshenko beam theory and MCST. Mollamahmutoğlu and Mercan (2019) analyzed the dynamic and static behavior of FG Timoshenko micro-beams considering different support conditions using MCST. Şimşek *et al*. (2013) conducted studies on static bending analysis of FG Timoshenko microbeams based on MCST. It is possible to find other studies in the literature that use MCST for static and dynamic analysis of nanostructures (Ansari *et al*. 2014, Lou *et al*. 2015, Nguyen *et al*. 2017a, b). Most of these presented approaches have either a strengthening or a weakening effect. For example, NT has a weakening effect and causes frequencies to decrease, while approaches such as MCST and SGT have a strengthening effect and cause frequencies to increase. The nonlocal modified couple stress theory (NMCST) considered in this study incorporates two different dimension parameters from both nonlocal and MCST into its formulations. Thanks to these dimension parameters, it is a more advanced approach as it is able to examine both strengthening and weakening aspects simultaneously. There are limited studies in the literature that perform static and dynamic analysis of nanostructures using non-local MCST (Abouelregal 2024, Attar *et al*. 2021, Ebrahimi and Barati 2018, Pham *et al*. 2023, Zheng *et al*. 2024).

In recent decades, machine learning (ML) algorithms have gained attention across various scientific fields, including engineering, environmental science, agriculture, medicine, and economics, due to their ability to identify patterns in data and make accurate predictions (Tariq *et al*. 2024a). In the context of nanotechnology, leveraging ML to study the material and structural properties of nano-structures is particularly important. ML can effectively predict the dynamic properties of nanobeams and offer new opportunities to enhance their performance and design. The application of ML in the study of nanostructures is thus becoming a key approach in advancing the field. Chen (2024) studied the vibration analysis of underwater nanobeams using decision and boosting tree regression algorithms. He found that these algorithms can provide accurate results while being efficient in terms of computational cost and time. Cheng *et al*. (2023) investigated the vibrational behavior of clamped-clamped FG porous nano-sized beams employing a neural network modeling approach. They trained the neural network model using the data obtained from third-order shear deformation beam theory and NSGT. Tariq *et al*. (2024b-e) applied various machine learning methodologies to study the dynamic properties of nanobeams. Tran *et al*. (2023) integrated the optimization technique with artificial neural network algorithm to study the buckling and vibration properties of porous microplates. Their hybrid machine learning model substantially saved computational costs without compromising accuracy. Le (2021) developed a Gaussian process regression model to estimate the tensile strength of polymer carbon nanotubes. The trained model

showed good performance on both training and testing datasets. Recently, other data-driven techniques such as physics-informed neural network (PINN) have gained wide popularity among researchers (Yu *et al*. 2024, Zhou *et al*. 2024). These methods implement physics of a problem as differential equations or penalty constraints in the loss function while training the model. Thus, the model not only learns relationships from the data but also makes predictions respecting these constraints, strengthening the performance and overall robustness of ML models (Eshkofti and Hosseini 2023, 2024a, b). The PINN model was trained by Yan *et al*. (2023) using extreme learning machine algorithm to predict the flexural response of nanoplates. They obtained the governing equations using second-order strain gradient theory.

A literature review reveals that while numerous studies have applied machine learning to analyze nanobeams using various theories, research on BD-FGNB based on NMCST remains scarce. Additionally, although artificial neural networks are widely used in the literature for modeling approaches, the application of state-of-the-art ensemble learning models for predicting the frequencies of FG nanobeams is still limited. It is essential to explore multiple ML models, as relying on a single model can lead to bias and result in less accurate predictions. This paper addresses these gaps through a comprehensive investigation and offers significant contributions to the field.

The objective of this work is to investigate the vibration behavior of BD-FGNB with deformable springs using both semi-analytical and machine learning approaches. The semi-analytical method employs Fourier sine series and Stokes' transform to address various boundary conditions, while size effects are modeled using nonlocal modified couple stress theory. The results from this approach are then used to train various supervised ML algorithms, including extreme gradient boosting, ANN, and decision tree regression, for predicting the natural frequencies in the first four vibration modes. The performance of these models is assessed against the semi-analytical results using multiple statistical metrics (R^2, MAE, MAPE, RMSE, A20-index) and visual tools such as scatter plots, radar plots, and Taylor diagrams. The study provides valuable insights by comparing the findings and leading to significant conclusions about the models' predictive performance.

2. Bi-directional FGM properties

In this study, the dynamic analysis of a BD-FGNB with lateral springs at its ends is carried out, as illustrated in Fig. 1. The BD-FGNB has a ceramic surface and a metal center, and the material properties change along the height and width directions as seen in Fig. 2. The changing material properties of nanobeam are shown as follows (Chen *et al*. 2013, Hassaine *et al*. 2024):

$$\phi(y,z) = \phi_s \Pi_s(y,z) + \phi_c \Pi_c(y,z) \tag{1}$$

where $\phi(y,z)$, ϕ_s and ϕ_c represent the composite, surface and center material properties of the FG nanobeam, respectively. $\Pi_s(y,z)$ and $\Pi_c(y,z)$ are the volume fractions of the surface and center components, respectively,

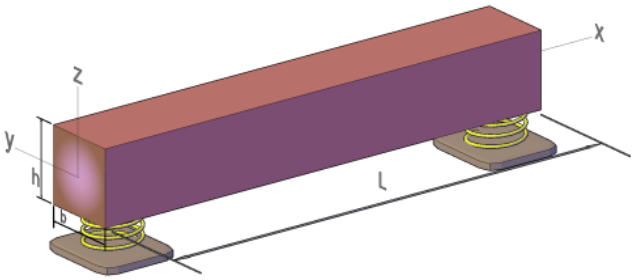

Fig. 1 The BD-FGNB restrained with transverse springs

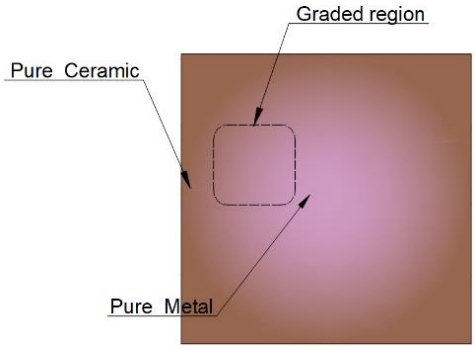

Fig. 2 Variation of material properties in BD-FGNB

and they are calculated as follows (Hassaine *et al*. 2024):

$$\Pi_s(y,z) = \left(1 - \left|\left|\frac{2y}{b}\right| - 1\right|\right)^g \left(1 - \left|\left|\frac{2z}{h}\right| - 1\right|\right)^p \tag{2}$$

$$\Pi_c(y,z) = 1 - \Pi_s(y,z) \tag{3}$$

Inserting the Eqs. (2) and (3) into Eq. (1):

$$\phi(y,z) = (\phi_s - \phi_c)\left(1 - \left|\left|\frac{2y}{b}\right| - 1\right|\right)^g \left(1 - \left|\left|\frac{2z}{h}\right| - 1\right|\right)^p + \phi_c \tag{4}$$

where g and p are the grading index parameters in y and z directions of BD-FGNB. Using Eq. (4), the effective Young's modulus, shear modulus, and mass density of the BD-FGNB $[E(y,z), G(y,z), \rho(y,z)]$ are derived as follows:

$$E(y,z) = (E_s - E_c)\left(1 - \left|\left|\frac{2y}{b}\right| - 1\right|\right)^g \left(1 - \left|\left|\frac{2z}{h}\right| - 1\right|\right)^p + E_c \tag{5}$$

$$G(y,z) = (G_s - G_c)\left(1 - \left|\left|\frac{2y}{b}\right| - 1\right|\right)^g \left(1 - \left|\left|\frac{2z}{h}\right| - 1\right|\right)^p + G_c \tag{6}$$

$$\rho(y,z) = (\rho_s - \rho_c)\left(1 - \left|\left|\frac{2y}{b}\right| - 1\right|\right)^g \left(1 - \left|\left|\frac{2z}{h}\right| - 1\right|\right)^p + \rho_c \tag{7}$$

3. Nonlocal modified couple stress theory

In this study, NMCST is considered for BD-FGNBs. At any point of the beam, the displacement component in the

x-direction is represented by u, while the displacement component in the z-direction is represented by w, and these parameters are shown as follows:

$$u(x,z,t) = -z\frac{\partial\psi(x,t)}{\partial x} \tag{8}$$

$$w(x,z,t) = \psi(x,t) \tag{9}$$

Here, $\psi(x,t)$ represents the transverse displacement of the elastic center, and t refers to time. The constitutive equations of the beam within the Cauchy stress tensor (σ_{ij}) and the couple stress tensor (m_{ij}) are expressed as below (Ma *et al*. 2008, Yang *et al*. 2002):

$$\sigma_{ij} = 2G(y,z)\varepsilon_{ij} + \varphi\varepsilon_{gg}\delta_{ij} \tag{10}$$

$$m_{ij} = 2l^2G(y,z)\chi_{ij} \tag{11}$$

where σ_{ij} represents the Cauchy stress tensor and m_{ij} is the couple stress tensor. The expressions δ_{ij} and l represent the Kronecker delta and material length scale parameter (MLSP), respectively. Moreover, Lame constants (G and φ) are obtained as below:

$$G(y,z) = \frac{E(y,z)}{2(1+v)} \tag{12}$$

$$\varphi = \frac{E(y,z)v}{(1+v)(1-2v)} \tag{13}$$

In addition, ε_{ij} and χ_{ij} represent the strain tensor and the symmetric curvature tensor, respectively, and are obtained as follows (Ma *et al*. 2008, Yang *et al*. 2002):

$$\varepsilon_{ij} = \frac{1}{2}\left(u_{i,j} + u_{j,i}\right) \tag{14}$$

$$\chi_{ij} = \frac{1}{2}\left(\theta_{i,j} + \theta_{j,i}\right) \tag{15}$$

The *v* in Eqs. (12) and (13) represents the Poisson's ratio. The θ_i in the above equations represents the rotation vector and is obtained as follows:

$$\theta_i = \frac{\varepsilon_{ijg}u_{g,j}}{2} \tag{16}$$

Here, u_i and ε_{ijg} are the components of the displacement vector and the permutation tensor, respectively. Inserting Eqs. (8) and (9) into Eqs. (14)-(16) yields the following equations:

$$\varepsilon_{xx} = -z\frac{\partial^2\psi(x,t)}{\partial x^2} \tag{17}$$

$$\chi_{xy} = -\frac{1}{2}\frac{\partial^2\psi(x,t)}{\partial x^2} \tag{18}$$

$$\theta_y = -\frac{\partial\psi(x,t)}{\partial x} \tag{19}$$

Substituting Eqs. (17)-(19) into Eqs. (10) and (11), the following equations are obtained (Ma *et al*. 2008, Yang *et al*. 2002):

$$\sigma_{xx} = -z[\varphi + 2G(y,z)]\frac{\partial^2\psi(x,t)}{\partial x^2} \tag{20}$$

$$\sigma_{yy} = \sigma_{zz} = -z\varphi\frac{\partial^2\psi(x,t)}{\partial x^2} \tag{21}$$

$$m_{xy} = -[l^2G(y,z)]\frac{\partial^2\psi(x,t)}{\partial x^2} \tag{22}$$

The nonlocal transformed differential constitutive relation is obtained as below (Ghandourah *et al*. 2021):

$$\sigma_{ij}^n - \gamma^2\nabla^2\sigma_{ij}^n = \sigma_{ij}^l \tag{23}$$

Here, σ_{ij}^l and σ_{ij}^n represent the local and nonlocal stress tensors, respectively, while γ^2 is the nonlocal parameter. In this study, the analysis of the Euler-Bernoulli beam, i.e., a thin beam with a high aspect ratio, is considered. In such thin beams, the Poisson effect is secondary and can be neglected to simplify the formulation of a simple beam theory (Park and Gao 2006). After this adjustment, all stresses except σ_{xx} are equal to zero (Park and Gao 2006, Pirmoradian *et al*. 2020). It should be noted that the formulations from this point onwards are derived in accordance with the aforementioned assumptions for thin beams. Considering Eqs. (20)-(22), the nonlocal constitutive relations of the nanobeam are derived as below (Ghandourah *et al*. 2021):

$$\sigma_{xx}^n - \gamma^2\nabla^2\sigma_{xx}^n = \sigma_{xx}^l \equiv -zE(y,z)\frac{\partial^2\psi(x,t)}{\partial x^2} \tag{24}$$

$$m_{xy}^n - \gamma^2\nabla^2 m_{xy}^n = m_{xy}^l \equiv -[l^2G(y,z)]\frac{\partial^2\psi(x,t)}{\partial x^2} \tag{25}$$

Hamilton's principle is frequently preferred in dynamic problems. Ghandourah *et al*. (2021) obtained the vibration expression and boundary conditions of porous functionally graded nanobeams based on NMCST using Hamilton's principle. The steps of obtaining the vibration expression and boundary conditions can be found in the work presented by Ghandourah *et al*. (2021). After performing the necessary mathematical operations and adjustments, the equation of motion for the BD-FGNB can be written as follows:

$$\begin{aligned}&-\gamma^2[\rho I]_{eff}\frac{\partial^6\psi}{\partial x^4\partial t^2} + \left([\rho I]_{eff} + \gamma^2[\rho A]_{eff}\right)\frac{\partial^4\psi}{\partial x^2\partial t^2}\\ &-[\rho A]_{eff}\frac{\partial^2\psi}{\partial t^2} - [EI]_{eff} + [GA]_{eff}l^2)\frac{\partial^4\psi}{\partial x^4} = 0\end{aligned} \tag{26}$$

At the points $x = 0$ and $x = L$, the nonlocal boundary conditions are as below (Ghandourah *et al*. 2021):

$$\begin{aligned}&-\gamma^2[\rho I]_{eff}\frac{\partial^5\psi}{\partial x^3\partial t^2} + \left([\rho I]_{eff} - \gamma^2[\rho A]_{eff}\right)\frac{\partial^3\psi}{\partial t^2\partial x}\\ &-([EI]_{eff} + [GA]_{eff}l^2)\frac{\partial^3\psi}{\partial x^3} = \bar{V}\end{aligned} \tag{27}$$

$$\begin{aligned}&\frac{\partial\psi}{\partial x} = \frac{\partial\overline{\psi}}{\partial x}\ or\\ &-\gamma^2[\rho I]_{eff}\frac{\partial^4\psi}{\partial x^2\partial t^2} + \gamma^2[\rho A]_{eff}\frac{\partial^2\psi}{\partial t^2} - ([EI]_{eff}\\ &+ [GA]_{eff}l^2)\frac{\partial^2\psi}{\partial x^2} = \bar{M}\end{aligned} \tag{28}$$

Here, $[EI]_{eff}$ and $[GA]_{eff}$ are the effective bending rigidity and shear rigidity, respectively, and they are defined

as follows:

$$[EI]_{eff} = \int_{-h/2}^{+h/2}\int_{-b/2}^{b/2} E(y,z)z^2 dydz \tag{29}$$

$$[GA]_{eff} = \int_{-h/2}^{+h/2}\int_{-b/2}^{b/2} G(y,z)dydz \tag{30}$$

In which, $[\rho I]_{eff}$ and $[\rho A]_{eff}$ are the effective mass moments of inertias and they are expressed as follows:

$$[\rho I]_{eff} = \int_{-h/2}^{+h/2}\int_{-b/2}^{b/2} \rho(y,z)z^2 dydz \tag{31}$$

$$[\rho A]_{eff} = \int_{-h/2}^{+h/2}\int_{-b/2}^{b/2} \rho(y,z)dydz \tag{32}$$

4. Applying solution procedure

In this part of the study, Fourier sine series and Stokes' transform are applied to the solutions of BD-FGNBs. The following equation is considered in the solutions:

$$\psi(x,t) = \Gamma(x)e^{i\omega t} \tag{33}$$

Here, ω is the frequency, and the relationship $i^2 = -1$ holds. Eq. (26) can be written by considering Eq. (33) as follows:

$$\begin{aligned}\gamma^2[\rho I]_{eff}\omega^2\frac{d^4\Gamma(x)}{dx^4} + \left([\rho I]_{eff} + \gamma^2[\rho A]_{eff}\right)\frac{\partial^4\Gamma(x)}{\partial x^2\partial t^2} \\ - [\rho A]_{eff}\frac{\partial^2\Gamma(x)}{\partial t^2} - ([EI]_{eff} \\ + [GA]_{eff}l^2)\frac{\partial^4\Gamma(x)}{\partial x^4} = 0\end{aligned} \tag{34}$$

Here, $\Gamma(x)$ represents the deflection function and is obtained as follows (Civalek *et al*. 2023):

$$\Gamma(x) = \begin{Bmatrix} \Gamma_0 & x = 0 \\ \Gamma_L & x = L \\ \sum_{j=1}^{\infty} B_j sin(\mu_j x) & 0 < x < L \end{Bmatrix} \tag{35}$$

Here, " $\mu_j = j\pi/L$ " and B_j represents the Fourier coefficient, which is derived as follows:

$$B_j = \frac{2}{L}\int_0^L \Gamma(x)sin(\mu_j x)dx \tag{36}$$

Taking the first derivative of Eq. (35) yields the following expression:

$$\Gamma'(x) = \sum_{j=1}^{\infty}\mu_j B_j cos(\mu_j x) \tag{37}$$

Eq. (37) can be obtained using the Fourier cosine series as follows:

$$\Gamma'(x) = \frac{b_0}{L} + \sum_{j=1}^{\infty} b_j cos(\mu_j x) \tag{38}$$

where b_0 and b_j represent Fourier constants and are obtained as below (Civalek *et al*. 2023):

$$b_0 = \frac{2}{L}\int_0^L \Gamma'(x)dx = \frac{2}{L}[\Gamma_L - \Gamma_0] \tag{39}$$

$$b_j = \frac{2}{L}\int_0^L \Gamma'(x)cos(\mu_j x)dx \quad (j = 1,2,\dots) \tag{40}$$

Using integration by parts on the term b_j in Eq. (52):

$$b_j = \frac{2}{L}[\Gamma(x)cos(\mu_j x)]_0^L + \frac{2}{L}\left(\mu_j\int_0^L \Gamma(x)sin(\mu_j x)dx\right) \tag{41}$$

$$b_j = \frac{2}{L}\left((-1)^j\Gamma_L - \Gamma_0\right) + \mu_j B_j \tag{42}$$

The derivatives of the deflection function $\Gamma(x)$ are calculated as follows (Civalek *et al*. 2023):

$$\Gamma'(x) = \frac{\Gamma_L - \Gamma_0}{L} + \sum_{j=1}^{\infty} cos(\mu_j x)\left[\frac{2\left[(-1)^j\Gamma_L - \Gamma_0\right]}{L} + \mu_j B_j\right] \tag{43}$$

$$\Gamma''(x) = -\sum_{j=1}^{\infty}\mu_j sin(\mu_j x)\left[\frac{2\left[(-1)^j\Gamma_L - \Gamma_0\right]}{L} + \mu_j B_j\right] \tag{44}$$

$$\begin{aligned}\Gamma'''(x) = \frac{\Gamma_L'' - \Gamma_0''}{L} + \sum_{j=1}^{\infty} cos(\mu_j x)\left[\frac{2\left[(-1)^j\Gamma_L'' - \Gamma_0''\right]}{L}\right. \\ \left. - {\mu_j}^2\left(\frac{2\left[(-1)^j\Gamma_L - \Gamma_0\right]}{L} + \mu_j B_j\right)\right]\end{aligned} \tag{45}$$

$$\begin{aligned}\Gamma^{(4)}(x) = -\sum_{j=1}^{\infty}\mu_j sin(\mu_j x)\left[\frac{2\left[(-1)^j\Gamma_L'' - \Gamma_0''\right]}{L}\right. \\ \left. - {\mu_j}^2\left(\frac{2\left[(-1)^j\Gamma_L - \Gamma_0\right]}{L} + \mu_j B_j\right)\right]\end{aligned} \tag{46}$$

$$\begin{aligned}\Gamma^{(5)}(x) = \frac{\Gamma_L^{(4)} - \Gamma_0^{(4)}}{L} \\ + \sum_{j=1}^{\infty} cos(\mu_j x)\left[\frac{2\left[(-1)^j\Gamma_L^{(4)} - \Gamma_0^{(4)}\right]}{L}\right. \\ \left. - \mu_j^2\left(\frac{2\left((-1)^j\Gamma_L'' - \Gamma_0''\right)}{L}\right) + \mu_j B_j)\right]\end{aligned} \tag{47}$$

$$\begin{aligned}\Gamma^{(6)}(x) = -\sum_{j=1}^{\infty}\mu_j sin\,(\mu_j x)\left[\frac{2\left[(-1)^j\Gamma_L^{(4)} - \Gamma_0^{(4)}\right]}{L}\right. \\ - \mu_j^2\left(\frac{2\left((-1)^j\Gamma_L'' - \Gamma_0''\right)}{L}\right) \\ \left. + \mu_j^4\left(\frac{2\left((-1)^j\Gamma_L - \Gamma_0\right)}{L}\right) + \mu_j B_j)\right]\end{aligned} \tag{48}$$

Substituting Eqs. (35), (44), and (46) into Eq. (34), the Fourier coefficient calculated as follows:

$$B_j = \frac{2\mu_j\left[\omega^2[\rho I]_{eff} + \gamma^2[\rho A]_{eff}\omega^2 + \left(-\left([EI]_{eff} + [GA]_{eff}l^2\right) + \gamma^2[\rho I]_{eff}\omega^2\right)\mu_j^2\right](\Gamma_0 - (-1)^j\Gamma_L)}{L\left[[\rho A]_{eff}\omega^2 + \left(\omega^2[\rho I]_{eff} + \gamma^2[\rho A]_{eff}\omega^2\right)\mu_j^2 + \left(-\left([EI]_{eff} + [GA]_{eff}l^2\right) + \gamma^2[\rho I]_{eff}\omega^2\right)\mu_j^4\right]} \quad (49)$$

The force boundary conditions can be written as follows:

$$-\gamma^2[\rho I]_{eff}\frac{\partial^5\psi}{\partial x^3\partial t^2} + \left([\rho I]_{eff} - \gamma^2[\rho A]_{eff}\right)\frac{\partial^3\psi}{\partial t^2\partial x} - ([EI]_{eff} + [GA]_{eff}l^2)\frac{\partial^3\psi}{\partial x^3}\Big|_{x=0} = S_0\Gamma_0 \quad (50)$$

$$-\gamma^2[\rho I]_{eff}\frac{\partial^5\psi}{\partial x^3\partial t^2} + \left([\rho I]_{eff} - \gamma^2[\rho A]_{eff}\right)\frac{\partial^3\psi}{\partial t^2\partial x} - ([EI]_{eff} + [GA]_{eff}l^2)\frac{\partial^3\psi}{\partial x^3}\Big|_{x=L} = -S_L\Gamma_L \quad (51)$$

Solving Eqs. (50) and (51) yields the following equations:

$$\left(-S_0 - \frac{[\rho A]_{eff}\gamma^2\omega^2}{L} + \frac{\omega^2[\rho I]_{eff}}{L} + \sum_{j=1}^{\infty}\frac{2L\omega^2[\rho A]_{eff}(\vartheta_3 - L^2\gamma^2\omega^2[\rho A]_{eff} + \vartheta_1)}{\vartheta_3 j^2\pi^2 + L^2\vartheta_2 + j^2\vartheta_1}\right)\Gamma_0 + \left(\frac{[\rho A]_{eff}\gamma^2\omega^2}{L} - \frac{\omega^2[\rho I]_{eff}}{L} - \sum_{j=1}^{\infty}\frac{2(-1)^jL\omega^2[\rho A]_{eff}(\vartheta_3 - L^2\gamma^2\omega^2[\rho A]_{eff} + \vartheta_1)}{\vartheta_3 j^2\pi^2 + L^2\vartheta_2 + j^2\vartheta_1}\right)\Gamma_L = 0 \quad (52)$$

$$\left(\frac{[\rho A]_{eff}\gamma^2\omega^2}{L} - \frac{\omega^2[\rho I]_{eff}}{L} - \sum_{j=1}^{\infty}\frac{2(-1)^jL\omega^2[\rho A]_{eff}(\vartheta_3 - L^2\gamma^2\omega^2[\rho A]_{eff} + \vartheta_1}{\vartheta_3 j^2\pi^2 + L^2\vartheta_2 + j^2\vartheta_1}\right)\Gamma_0 + \left(-S_L - \frac{[\rho A]_{eff}\gamma^2\omega^2}{L} + \frac{\omega^2[\rho I]_{eff}}{L} + \sum_{j=1}^{\infty}\frac{2L\omega^2[\rho A]_{eff}(\vartheta_3 - L^2\gamma^2\omega^2[\rho A]_{eff} + \vartheta_1)}{\vartheta_3 j^2\pi^2 + L^2\vartheta_2 + j^2\vartheta_1}\right)\Gamma_L = 0 \quad (53)$$

where,

$$\vartheta_1 = (j^2\pi^2\gamma^2\omega^2 + L^2\omega^2)[\rho I]_{eff} \quad (54)$$

$$\vartheta_2 = (j^2\pi^2\gamma^2\omega^2 + L^2\omega^2)[\rho A]_{eff} \quad (55)$$

$$\vartheta_3 = -\left([EI]_{eff} + [GA]_{eff}l^2\right)j^2\pi^2 \quad (56)$$

In which, S_0 and S_L represent the lateral spring coefficients of the BD-FGNBs. Eqs. (52) and (53) can be written in matrix form as:

$$\begin{bmatrix}\Omega_{11} & \Omega_{12}\\ \Omega_{21} & \Omega_{22}\end{bmatrix}\begin{bmatrix}\Gamma_0\\ \Gamma_L\end{bmatrix} = 0 \quad (57)$$

Matrix components are specified in the Appendix. The eigenvalues derived from the expression below give the natural frequencies of the BD-FGNBs.

$$\begin{vmatrix}\Omega_{11} & \Omega_{12}\\ \Omega_{21} & \Omega_{22}\end{vmatrix} = 0 \quad (58)$$

5. Overview of the machine learning methodology

Different machine learning models have unique strengths, which lead to different performances on the same datasets due to their distinct characteristics. Selecting the most appropriate model for a given problem is crucial. In this study, three ML models—namely, Extreme Gradient Boosting (XGB), Artificial Neural Network (ANN), and Decision Tree Regression (DTR)—were employed to predict the transverse (lateral) frequencies of a BD-FGNB. A brief outline of these models is presented below.

5.1 Extreme gradient boosting (XGB)

XGB is a tree-based ensemble learning methodology that has gained significant popularity in recent years due to its robust performance and efficiency. Chen and Guestrin (2016) developed this methodology to efficiently implement gradient-boosting algorithm introduced by Friedman *et al*. (2000). The great problem-solving abilities and inexpensive prerequisites of XGB have found its application in various industrial and scientific areas. The XGB algorithm enhances prediction accuracy by combining various weak models with other training techniques. It deals with the overfitting issues by including the regularization parameters and the second-order Taylor series expansion in the loss function. The objective function is mathematically expressed as:

$$\mathcal{L} = \sum_i \varkappa(y_i, \hat{y}_i) + \sum_m \Omega(f_m) \quad (59)$$

where $\varkappa$ represents the loss function, y_i and $\hat{y}_i$represents the actual and predicted values, respectively. Ω denotes a regularization penalty for the f_m model. $\Omega(f_m)$ is expressed as follows:

$$\Omega(f_m) = \Upsilon T + \frac{1}{2}\lambda\|\omega\|^2 \quad (60)$$

Here, Υ and λ are the constants to control the model's complexity, T represents the number of leaves and ω denotes the sum of leaf weights. During XGB model

training, the two most critical parameters that affect the model performance are the number of estimators (trees) and tree depth. A higher number of estimators is generally required when training the model for complex problems, and a larger tree depth is used to enhance the model's accuracy. These parameters should be selected carefully to avoid overfitting the model.

5.2 Artificial neural network (ANN)

ANN is a human brain-inspired ML model that uses interconnected nodes in a layered structure similar to the neurons in the brain. ANNs learn information by identifying patterns within the data. An ANN is made of input, hidden and output layer, all of which are interconnected by neurons. Once the ANN model is constructed, the most commonly used back-propagation methods is implemented to learn information from the data (Agatonovic-Kustrin and Beresford 2000). The input data is fed forward through the network of layers to optimize the weights across all the neurons. Throughout the training process, the errors calculated at the outputs are back propagated to optimize the weights and reduce the difference between the actual and predicted data. The model training cycle continues until the prediction error is minimized and the network obtains desired level of accuracy. ANN model's input-output relationship can be expressed as follows:

$$y = f\left(W^{(L)}.f\left(W^{(L-1)}.f\left(\ldots f\left(W^{(1)}.x + b^{(1)}\right) + b^{(L-1)}\right)\right) + b^{(L)}\right) \tag{61}$$

where, x and y are the input and output vectors, L is the number of layers, $W^{(n)}$ and $b^{(n)}$ represents the weight matrix and the bias vector for layer n, respectively. $f(\,)$ is the applied activation function.

5.3 Decision tree regression (DTR)

DTR is a hierarchical tree-based ML technique used for making predictions for both classification and regression problems. DTR remains a popular choice for modeling complex relationships in data due to its simplicity and interpretability features. The DTR algorithm splits the dataset into a tree-like structure with three main elements, the root node, internal nodes, and leaf node. A root node denotes the dataset, and each internal node in the DTR model tests a particular feature to help differentiate between classes. The ultimate result of this test is then signified by the leaf node. It estimates values by repeatedly dividing the data into subsets according to the feature values that minimize errors. The process of splitting the data terminates after the predetermined minimum node size is obtained (Xu *et al*. 2005). Error function, tree depth, sample split and sample leaf are a few DTR parameters that influence the accuracy of prediction. The error function minimizes the difference between the actual value and predicted value. The tree depth determines the size of the tree; more complex and nonlinear problems require deeper trees to capture additional information. The parameters for sample split and sample leaf specify the sample sizes needed for splitting an internal node and to remain at a leaf node, respectively. These parameters need to be optimized well in order to get the best outputs.

5.4 Performance evaluation metrics

The performance of trained ML models is evaluated by testing them on previously unseen testing data. For this purpose, five statistical metrics are used for each model. These metrics include the coefficient of determination (R2), Mean Absolute Error (MAE), Root Mean Squared Error (RMSE), Mean Absolute Percentage Error (MAPE), and A20-index.

$$R^2 = 1 - \frac{\sum_{i=1}^{n}(y_i - \widehat{y_i})^2}{\sum_{i=1}^{n}(y_i - \bar{y})^2} \tag{62}$$

$$MAE = \frac{1}{n}\sum_{i=1}^{n}|(y_i - \widehat{y_i})| \tag{63}$$

$$MAPE = 100 \times \frac{1}{n} \times \sum_{i=1}^{n}\left|\frac{y_i - \widehat{y_i}}{y_i}\right| \tag{64}$$

$$RMSE = \left[\frac{1}{n}\sum_{i=1}^{n}(y_i - \widehat{y_i})^2\right]^{1/2} \tag{65}$$

$$A20 - Index = \frac{1}{n}\sum_{i=1}^{n}\begin{cases}1, & if\ \dfrac{|y_i - \widehat{y_i}|}{y_i} \le 0.2\\ 0, & otherwise\end{cases} \tag{66}$$

In these equations, i denotes the index of each observation, y_i represents the actual output value, $\widehat{y_i}$ denotes the predicted output value, and $\bar{y}$ is the mean of all the observations. R^2, also known as the coefficient of determination measures a fit quality in a ML model, ranging from 0 (poor fit) to 1 (strong fit). MAE is a simple accuracy measure that indicates the average absolute difference between actual and predicted values. MAPE is the percentage equivalent of MAE that shows the prediction accuracy relative to actual values in percentage. RMSE computes the square root of the average squared differences between actual and predicted data. The A20-index represents the percentage of predictions that fall within a deviation of ±20% from the actual values. The index ranges from 0 to 1, with higher scores indicating better predictive accuracy, as more predictions are closer to the actual values.

6. Data generation for ML model training

The vibrational behavior of the BD-FGNB is significantly influenced by several key parameters, including the material grading index along the width and height directions (g and p, respectively), the length of the nanobeam (L), the MLSP (l), and the nonlocal parameter (γ). Understanding how these factors influence the natural frequencies of nanobeams is essential for accurate modeling

Table 1 Nanobeam parameter limits

Parameters	Gradition Index Width (g)	Gradition Index Height (p)	Nanobeam Length (L)	MLSP (l)	Nonlocal Parameter (γ)
Minimum	0	2	5h	0	0
Maximum	20	20	50h	2h	2h

Table 2 Training dataset of symmetric porous nanobeam

g	p	L	l	γ	ω_1 (E+09)	ω_2 (E+09)	ω_3 (E+09)
0.46	7.79	81.90	1.28	4.32	9.99470	38.3984	81.2640
6.39	19.7	114.8	4.22	5.28	4.17820	16.2081	34.7776
12.58	8.28	34.17	2.55	4.68	43.4816	142.175	254.543
1.76	3.01	41.23	5.93	5.57	37.0721	121.978	219.907
19.7	1.63	19.59	2.01	1.83	139.849	488.577	915.517
5.20	14.5	142.6	2.99	4.22	2.75070	10.8582	23.9139

Table 3 Descriptive statistics of input features and outputs

Data Sets		g	p	L	l	γ	ω_1 (E+09)	ω_2 (E+09)	ω_3 (E+09)
Training	X_{min}	0.0006	0.0004	15.004	0.0002	0.0003	2.41327	9.44755	20.5194
	X_{ave}	9.98	10.004	82.506	3.003	3.0	23.6467	82.3005	161.245
	X_{max}	19.99	19.999	149.99	5.999	5.999	316.970	1050.79	2229.70
	σ	5.777	5.773	39.004	1.728	1.734	36.7565	120.145	225.405
Testing	X_{min}	0.0058	0.0122	15.03	0.0017	0.0024	2.41049	9.50966	20.8219
	X_{ave}	10.07	9.9869	82.471	2.985	2.997	23.8366	83.0681	162.934
	X_{max}	19.99	19.992	149.96	5.993	5.994	272.100	1001.11	1987.13
	σ	5.755	5.772	38.843	1.745	1.722	37.7734	123.773	232.515
All data	X_{min}	0.0006	0.0004	15.004	0.0002	0.0003	2.41049	9.44755	20.5194
	X_{ave}	10.0	10.0	82.499	3.0	3.0	23.6847	82.4540	161.583
	X_{max}	19.99	19.999	149.99	5.999	5.999	316.970	1050.79	2229.70
	σ	5.773	5.773	38.972	1.732	1.731	36.9623	120.880	226.846

and analysis. Therefore, these five parameters are selected as input features of machine learning models, and the database is generated by changing their values. Additionally, the stiffness of the springs at both ends of the BD-FGNB is equal and $S_0=S_L=10_7$ nN/nm for the generated dataset.

The performance of ML models greatly depends on both the quantity and quality of the data samples used. Therefore, it is important to choose a reliable sampling technique that ensures a random and uniform distribution of feature samples. Among the various sampling methods, a type of quasi-random sampling method called Sobol sequence sampling is commonly used for sensitivity analyses. This method generates parameter values that are uniformly distributed across multi-dimensional spaces with minimum data clusters and gaps (Renardy *et al*. 2021). In this study, Sobol sequence sampling was employed to thoroughly explore the design space of input parameters and examine their relationship with the natural frequencies of nanobeams. The minimum and maximum values for the nanobeam parameters used in Sobol sampling are provided in Table 1.

A total of 16,386 data samples were generated using the Sobol sampling method, covering various combinations of the input features within the limits specified in Table 1. The samples were generated by selecting the parameter m = 14 for the Sobol method, which calculates the number of samples as 2^m. The generated samples exhibited a very low discrepancy value of 1.786E-7, indicating a well-distributed and uniform coverage of the parameter space. This uniformity of the dataset is critical for effectively training machine learning models. Increasing m to 15 would double the number of samples to 32,768 and slightly improve the models' performance. However, this would come at the cost of significantly higher computational requirements. Larger datasets require longer training times and increase the computational effort for hyperparameter tuning, which involves repetitive training iterations to identify optimal model configurations. Therefore, the chosen dataset size was deemed sufficient to achieve the high accuracy demonstrated by our models without incurring excessive computational costs and training times.

Nonlocal modified couple stress theory is used to calculate the frequency of the nanobeam for each data sample. The accuracy of the semi-analytical results is critical for the effectiveness of the ML predictions because the generated dataset forms the foundation upon which the machine learning models are trained and validated. Any inaccuracies in the semi-analytical results could propagate into the training process, leading to reduced predictive

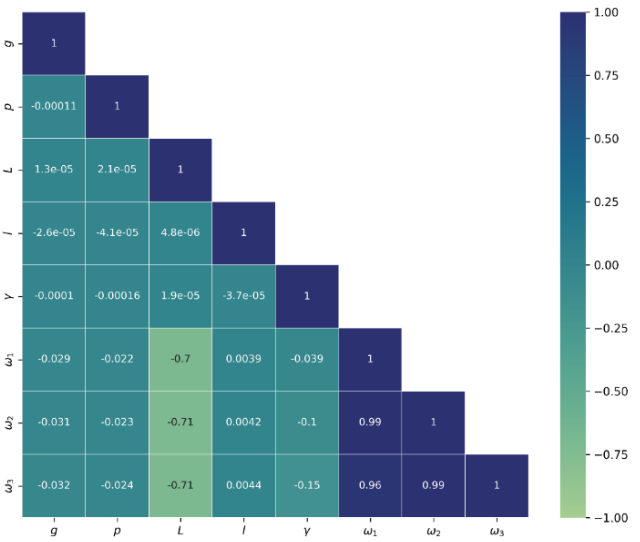

Fig. 3 Correlation between input features and frequencies of nanobeam

Table 4 The optimal hyperparameters of ML models

Model	Hyperparameters	Optimal Value
XGB	Booster	Gbtree
	No. of estimators	300
	Maximum depth	7
	Learning rate	0.05
	Subsample	1
	Sampling method	Uniform
ANN	Optimizer	Adam
	Learning rate	0.001
	No. of hidden layers	3
	No. of neurons per layer	64
	Activation function	Relu
	Loss function	Mean squared error
	Epochs	500
	Batch size	64
DTR	Criterion	Squared error
	Maximum depth	12

performance of the ML models. Therefore, ensuring the reliability and fidelity of the semi-analytical solutions is essential to enable the ML models to accurately capture the underlying physical behavior of the system and deliver trustworthy predictions. The nanobeam considered in this study has dimensions of 3 nm in both width and height, with Young's modulus of 380 GPa at the outer surface (EE_u) and 70 GPa at the outer center (EE_a). The resulting frequencies of the first three vibration modes for each sample are stored in the dataset. The first six rows of the dataset with input features and the corresponding frequencies outputs are presented in Table 2.

In this study, Pearson correlation coefficient (PCC) is employed to evaluate the influence of input features on the vibrational frequencies of the BD-FGNB. The PCC is a statistical tool that quantifies the linear relationship between two variables. It ranges from -1 (denoting strong negative correlation) to +1 (denoting strong positive correlation), with 0 indicating no linear relationship. The corresponding PCC results are shown in Fig. 3. This figure shows that the nanobeam length (L) has a significantly strong negative correlation coefficient of -0.7 with all vibration modes. This strong negative correlation between L and frequency aligns with the fundamental principles of structural dynamics, where the natural frequency of a beam is inversely proportional to its length. Longer beams exhibit lower stiffness relative to their mass, directly resulting in reduced natural frequencies. On the other hand, the weak correlation of 0.0039 between the MLSP and frequency highlights the limited influence of the size-dependent material properties on the overall vibration characteristics within the studied parameter range. Notably, the correlation between MLSP and frequency shows a slight increase in higher vibration modes, reaching up to 0.0044 in the third mode. This suggests that size effects become marginally more significant at higher frequencies. Additionally, the nonlocal parameter (γ) shows an increasingly negative correlation with the frequencies as the vibration modes increase. Overall, this correlation matrix suggests that the nanobeam length is the primary governing factor in frequency predictions.

7. Modeling results

7.1 Optimal model configurations

Each machine learning model undergoes an extensive hyperparameter tuning process through manual adjustments. The optimal hyperparameter values to maximize model performance are determined by the trial-and-error approach. A seed value of 20242303 is employed to ensure reproducibility and fair comparison during the tuning process. The ideal hyperparameters for each model are detailed in Table 4, while any unspecified hyperparameters are kept at their default settings.

7.2 Performance evaluation of ML models

In this section, a detailed analysis of the results generated by the machine learning models on both the training and testing datasets is provided. The aim is to evaluate the accuracy and generalization capabilities of these models in predicting the natural frequencies of nanobeams. As mentioned earlier, the performance of the models has been assessed using five statistical metrics: R^2, MAE, MAPE, RMSE, and A20-index. Tables 5, 6, and 7 present the evaluation metrics for all ML models across the training and testing sets for the first, second, and third vibration modes, respectively.

It can be observed from the tables that all models demonstrate strong performance across each vibration mode according to the evaluation metrics. The A20-index of 1 in nearly all cases suggests that 100% of the model predictions fall within a ±20% deviation from the actual values. This denotes that the predicted and actual values are very close

Table 5 Performance metrics of all models for mode 1

Model	Dataset	R^2	MAE	MAPE	RMSE	A20-Index
XGB	Training	0.9999	128172691.0	0.0054	287074183.6	1
	Testing	0.9985	407747996.9	0.0094	1452030591.8	1
ANN	Training	0.9999	161314181.1	0.0115	289515469.6	1
	Testing	0.9999	177260796.3	0.0116	366479762.2	1
DTR	Training	0.9998	219999077.6	0.0145	476845691.1	1
	Testing	0.9899	1136358288.5	0.0325	3721493601.9	0.9936

Table 6 Performance metrics of all models for mode 2

g	Dataset	R^2	MAE	MAPE	RMSE	A20-Index
0.46 6.39	Training	0.9999	448405874.7	0.0055	936845032.6	1
	Testing	0.9974	1627498762.9	0.0106	6214603620.3	1
12.58 1.76	Training	1	490891609.7	0.0106	791665909.2	1
	Testing	0.9999	563546956.9	0.0111	1160045723.1	1
19.7 5.20	Training	0.9999	732092464.2	0.0143	1439374701.0	1
	Testing	0.9895	3983382716.8	0.0340	12423683292.8	0.9921

Table 7 Performance metrics of all models for mode 3

g	Dataset	R^2	MAE	MAPE	RMSE	A20-Index
0.46 6.39	Training	0.9999	909883032.4	0.0058	1822957946.7	1
	Testing	0.9970	3292335443.0	0.0113	12622880954.1	1
12.58 1.76	Training	0.9999	1163003951.2	0.0110	2040268967.9	1
	Testing	0.9998	1305188753.9	0.0114	2974612428.4	1
19.7 5.20	Training	0.9998	1835627402.6	0.0172	3550993947.0	1
	Testing	0.9876	8477058030.1	0.0384	25275124252.9	0.9905

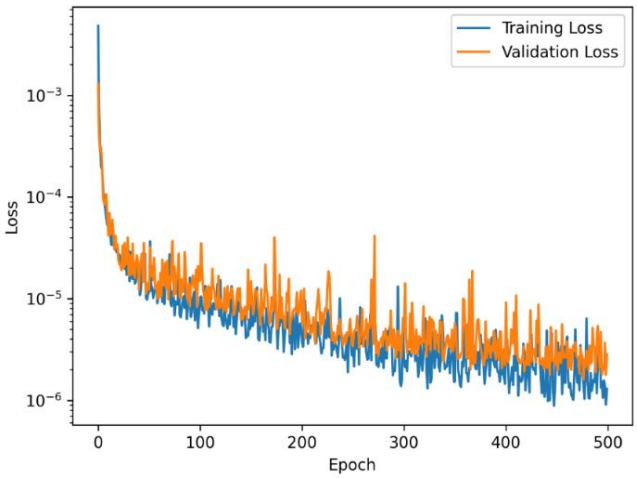

Fig. 4 Training plot of ANN model

to each other. The XGB, ANN, and DTR models show excellent performance with high R^2 values across all three modes. This high R^2 indicates that these models fit the data well and explain a significant portion of the variance in the output. However, ANN shows more consistent results between the training and testing datasets, indicating better generalization capability. In contrast, XGB and DTR exhibit slight overfitting, as shown by lower R^2 values on the testing data. While XGB achieves the lowest MAE, MAPE, and RMSE values on the training set, these values increase significantly on the testing set due to overfitting. On the other hand, the ANN model maintains low and consistent MAE, MAPE, and RMSE values across both datasets, confirming its superior performance among all models.

The ANN training plot, representing the loss curves for both the training and validation datasets over 500 epochs, is illustrated in Fig. 4. Both curves show a steady decrease in loss as the number of epochs increases, indicating that the model is effectively learning the underlying patterns in the data.

Importantly, the training and validation curves closely overlap during the model training, indicating the absence of overfitting. The steady decrease in both training and validation loss, along with their close alignment, indicates that the model is generalizing well to unseen data.

A holistic comparison of the XGB, ANN, and DTR models across different metrics for the training and testing datasets is illustrated in Fig. 5 using radar plots. In these plots, a smaller enclosed area represents better model performance. When comparing Figs. 5(a) and 5(b), it can be seen that the MAE, MAPE and RMSE values increase on the testing dataset for the XGB and DTR model. This indicates slight overfitting by XGB and significant overfitting by DTR. In contrast, the area enclosed by the

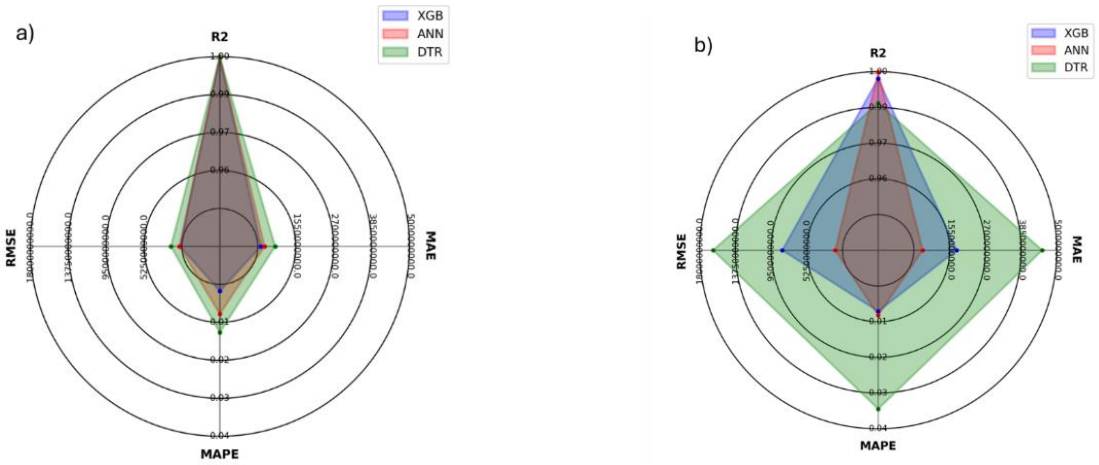

Fig. 5 Radar plots of all ML models for a) training and b) testing dataset

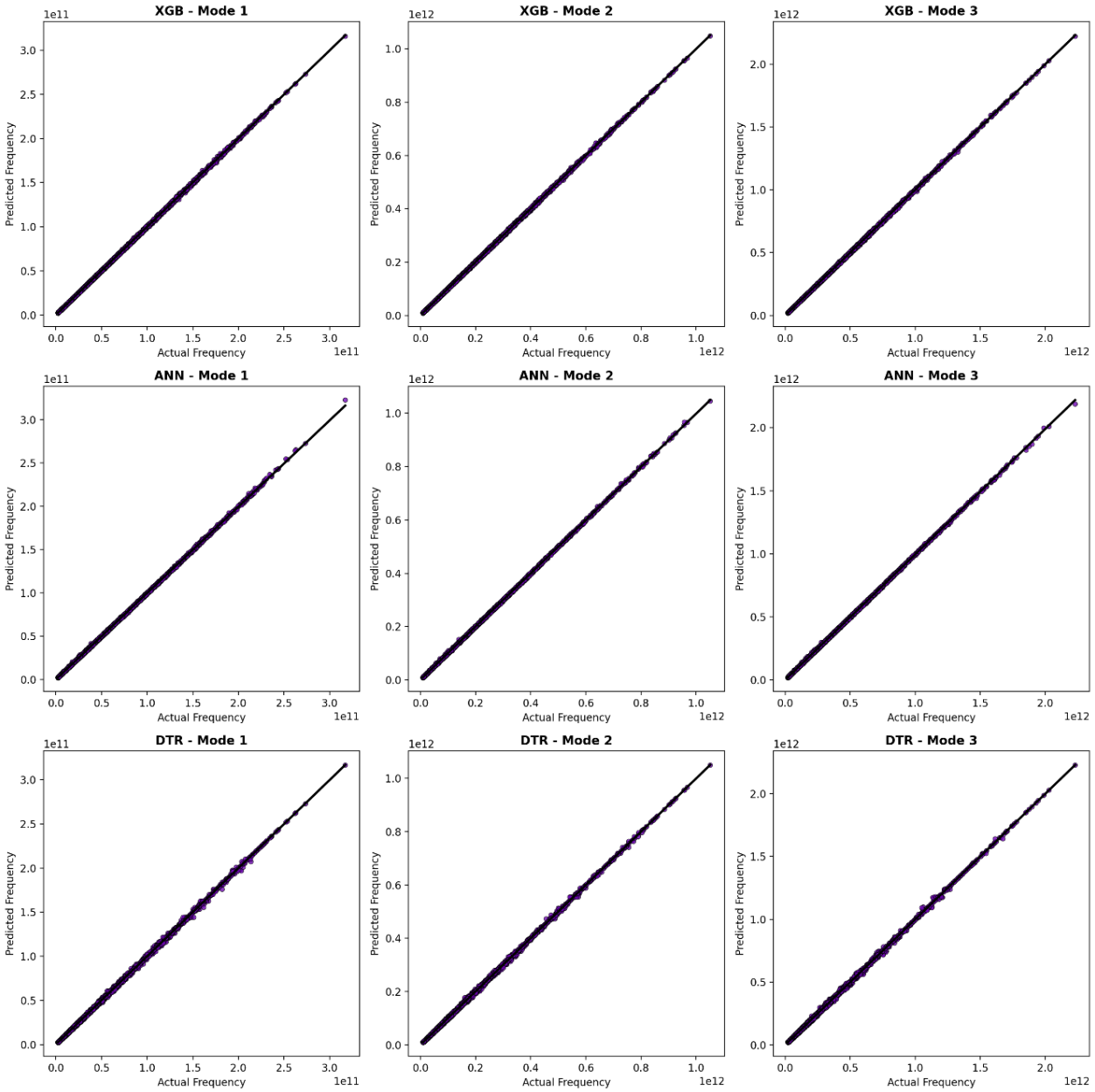

Fig. 6 Scatter plots of XGB, ANN and DTR for the testing dataset

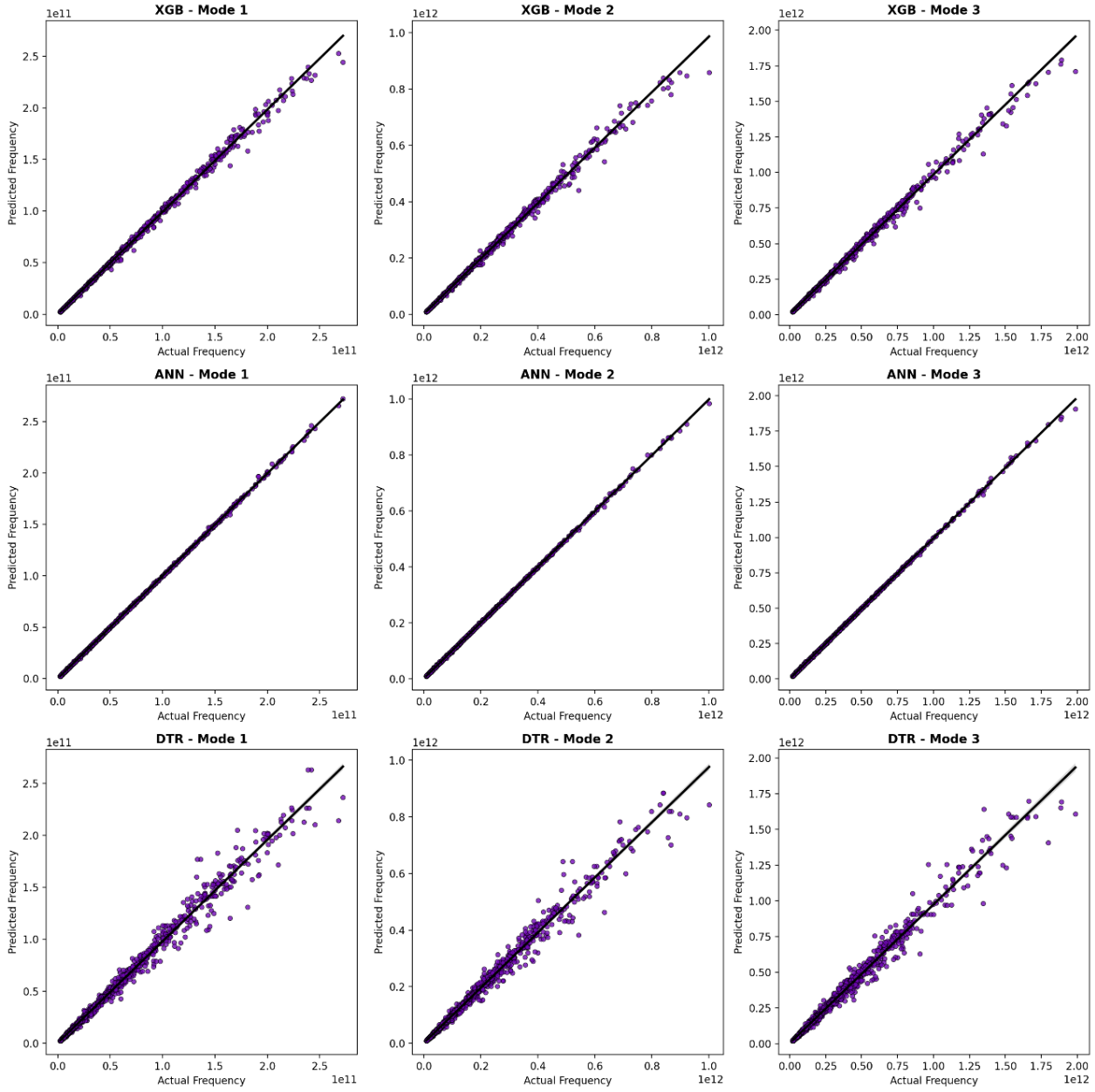

Fig. 7 Scatter plots of XGB, ANN and DTR for the testing dataset

ANN model remains nearly unchanged between the training and testing datasets and is the smallest among all models.This suggests that the ANN model delivers more consistent and accurate predictions of the vibration frequencies for functionally graded nanobeams.

The scatter plots in Figs. 6 and 7 to visually illustrate how much the actual and predicted values deviate from each other. In Fig. 6, most data points align closely with the 45-degree diagonal line across all three vibration modes for the training dataset. This means the predicted and actual values are in good agreement with each other. Hence, all the models predicted frequencies with very high accuracy on the training data. However, it can be seen in Fig. 7 that there is a slight dispersion exhibited by XGB and a more significant dispersion of data points exhibited by DTR. The frequencies predicted by XGB and DTR deviate more significantly from the actual values on the testing dataset compared to the training dataset. Among the three models, the ANN model demonstrated excellent performance on the testing dataset, with predictions closely following the diagonal line across all modes.

The Taylor diagram is a popular graphical tool for assessing ML models based on key metrics like the correlation coefficient and standard deviation. Fig. 8 presents the Taylor diagrams for the XGB, ANN, and DTR models, evaluated on both the training and testing datasets across the three vibration modes. It can be seen in Fig. 8a that all models cluster closely near the reference point (REF), indicating a high degree of accuracy on the training dataset. The standard deviations of the models are also low, and the correlation values are nearly equal to 1. This indicates that the models have effectively learned the

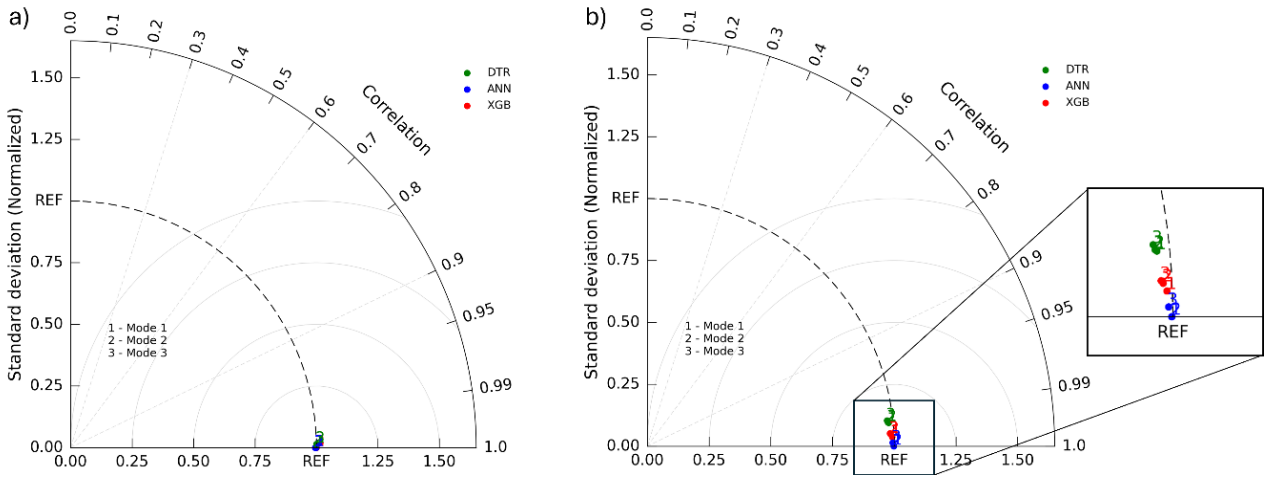

Fig. 8 The Taylor diagrams of all models for a) training and b) testing dataset.

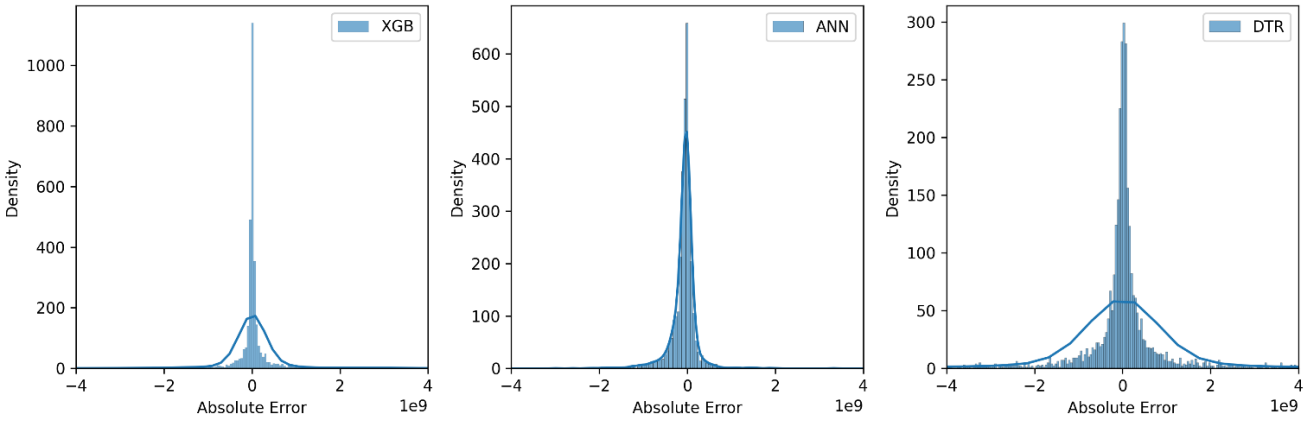

Fig. 9 Prediction error distribution plots of all ML models for testing dataset

relationships in the training data and predictions are well aligned with the actual data. For the testing dataset in Fig. 8b, the XGB and DTR models show slightly higher standard deviations and lower correlation values compared to their performance on the training dataset. This indicates a minor drop in performance and slight overfitting. However, the ANN model remains very close to the REF point across all three modes, demonstrating strong generalization and high accuracy even on the testing data.

The error distribution plots from all the ML models for the first vibration mode of the nanobeam is illustrated in Fig. 9. It can be observed from these error distribution plots that peak error density of all three models is concentrated around zero, but the distribution characteristics differ significantly. ANN has the highest density peak at zero error compared to XGB and DTR and exhibits the narrowest spread of errors, as seen from the smaller density tails. This implies that ANN provides the most consistent predictions with lower variance in error. XGB's density peak is lower than ANN's but still higher than DTR, indicating reasonably good predictions. DTR, on the other hand shows the widest spread of errors, lowest peak and the least steep curve among the three models. This suggests that DTR might not generalize as well to the test data and is prone to larger prediction errors.

The superior performance of the ANN model compared to XGB and DTR in predicting the vibration frequencies of nanobeams can be attributed to its multi-layer architecture and the backpropagation mechanism, which enables effective learning of complex and non-linear relationships. This allowed ANN to capture the intricate dependencies inherent in the dynamic analysis of the BD-FG nanobeams more effectively than ensemble-based models like XGB or rule-based models like DTR. However, it is important to note that ANN may not consistently outperform other models across all engineering problems. The performance of ML models depends on various factors, including the complexity of the problem, the model's architecture, and its data handling characteristics. Therefore, it is essential to employ multiple ML models in modeling studies to conduct a thorough comparative analysis. Relying solely on the performance of a single ML model may lead to bias or inaccurate results (Demšar 2006).

One of the reasons for the discrepancies in predictive accuracy across vibration modes is related to the increasing complexity of higher modes. The frequency values in higher modes (e.g., the second and third modes) are significantly larger than those in the lower modes. For instance, the frequency values for the third mode exhibit an increase of over 600% compared to the first mode in the

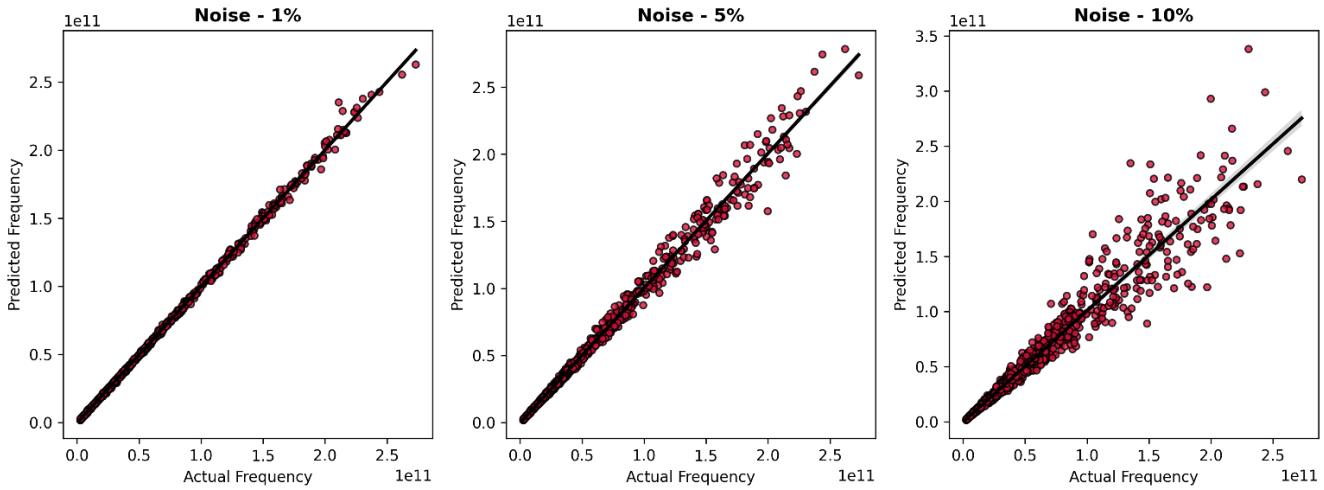

Fig. 10 Sensitivity of the ML model to various levels of noises.

majority of the samples in the dataset. This substantial difference can amplify the error values in metrics like MAE and RMSE for higher modes. However, it is important to note that the relative accuracy of the models, as reflected in metrics like R^2 and MAPE, remains high and comparable to the performance observed in the lower modes. This indicates that the models still capture the underlying patterns effectively, despite the apparent increase in absolute error values.

7.3 Computational efficiency analysis

The ML models were developed using Python 3.11 and trained on a system equipped with a 12th Gen Intel® Core™ i9-12900H processor operating at 2.5 GHz and 64 GB of RAM. The computational time required for training each model varied significantly, reflecting differences in their algorithmic complexity and parameter optimization processes. Specifically, the XGB model required approximately 42.2 seconds, the ANN model took 312.7 seconds, and the DTR model completed training in just 15 seconds.

The ANN model, while achieving the highest predictive accuracy, incurred the longest computation time due to its iterative backpropagation process and the need to optimize a large number of parameters across multiple layers. Conversely, the DTR model demonstrated the shortest training time owing to its simpler tree-based structure but was less robust in predictive accuracy. The XGB model, which uses an ensemble learning approach, balanced computation time and accuracy effectively.

7.4 Noise sensitivity analysis

A noise sensitivity analysis is conducted to evaluate the robustness of the trained ANN model under various noise levels. This approach aimed to simulate conditions where input features might be prone to measurement errors or uncertainties, as often encountered in practical applications. Therefore, artificial noise was introduced into the dataset at three different levels: low noise (1%), moderate noise (5%), and high noise (10%). The noise was generated as Gaussian noise proportional to each feature's standard deviation, ensuring variability in the dataset. The model's performance was then assessed by examining its ability to predict the natural frequencies of nanobeams under these noisy conditions, as shown in Figure 10.

The results demonstrate that the ANN model is robust to noise at low and moderate levels, with a gradual degradation in performance as the noise level increases. At 1% noise, the model achieved an excellent R2 value of 0.999, indicating a nearly perfect agreement between the actual and predicted values. The scatter plot for this case shows minimal deviations, with predictions clustering tightly along the diagonal line. Under moderate noise conditions (5%), the model maintained a high R2 value of 0.992, with a slight increase in the scatter between actual and predicted frequencies. This indicates a small drop in prediction accuracy. For the high noise scenario (10%), the R2 value decreased to 0.961, and the scatter plot revealed noticeable discrepancies between predictions and actual values. The discrepancies are more significant at the higher frequency values of the nanobeam. While the performance drop at higher noise levels is expected, the model's ability to maintain a high R2 value and provide reasonable predictions under such conditions underscores its applicability for many practical scenarios.

8. Numerical applications based on the analytical solution

In this part of the study, the eigenvalue problem obtained by the solution method based on Fourier series and Stokes' transformation is used to analyze BD-FGNBs. Unless otherwise stated, the geometrical and material properties used in these analyses are as follows: $E_s = 380\ GPa$, $E_c = 70\ GPa$, $\upsilon_s = \upsilon_c = 0.3$, $\rho_s = 3960\ kg/m^3$, $\rho_c = 2702\ kg/m^3$, $b = h = 3\ nm$, $g = p = 1$, $L = 20h\ nm$. The number of terms (j) in the analytical solution is considered as 20. Also, the stiffness of the springs at both ends of the BD-FGNB is equal and $S_0 = S_L = 10^7\ nN/nm$.

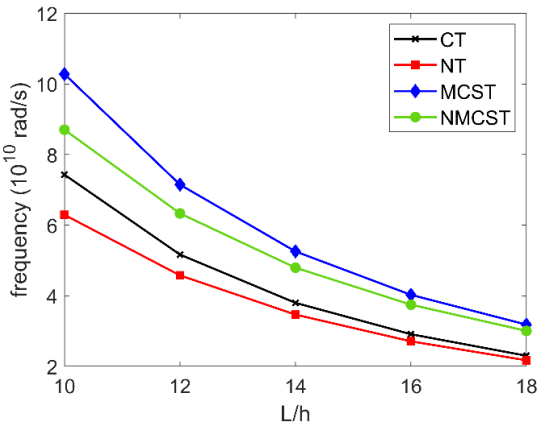

Fig. 11 Effect of *L/h* for different theories

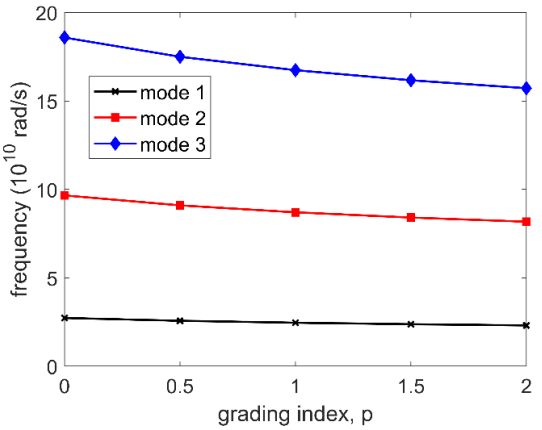

Fig. 12 Effect of grading index *p*

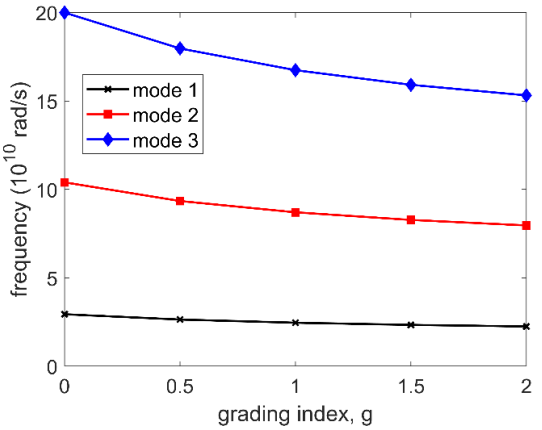

Fig. 13 Effect of grading index *g*

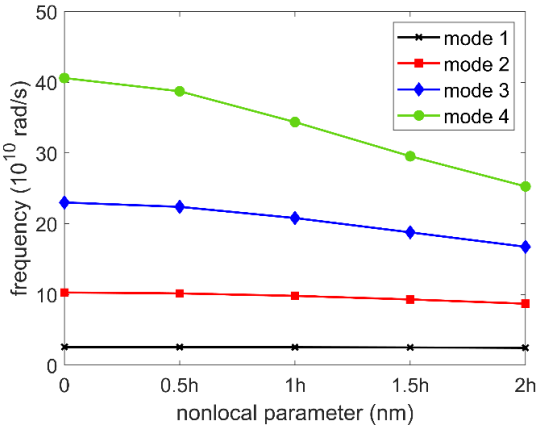

Fig. 14 Effect of γ on vibrational modes

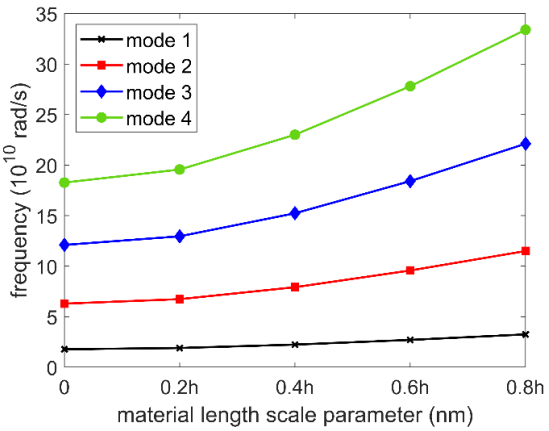

Fig. 15 Effect of l on vibrational modes

In Fig. 11, the influence of various *L/h* ratios, ranging from 10 to 18, on frequencies is analyzed for different theories. The NMCST studied in this work is a combination of two different higher-order theories (NT and MCST). This means that when γ in the theory is neglected, the results of the MCST are obtained, when l is neglected, the results of the nonlocal theory are obtained, and finally, when both γ and l are neglected, the results of the classical theory are obtained. In this section, the following parameters are used for the theories compared:

for CT: γ=*l*=0 nm
for NT: γ=2h nm, *l*=0 nm
for MCST: γ=0 nm, *l*=0.5h nm
for NMCST: γ=2h nm, *l*=0.5h nm

It is obvious from Fig. 11 that increasing the *L/h* ratio causes the frequencies of the BD-FGNB to decrease. This decrease is valid for all theories. From this figure, the frequency values of the theories can be easily compared. As can be seen, the highest ω values are obtained with MCST, while the lowest frequencies are obtained with NT.

Fig. 12 shows the impact of the grading index *p*, while Fig. 13 shows the effect of grading index *g*. When analyzing the frequency values of the BD-FGNB for the first three modes, the grading indexes are considered at various values from 0 to 2. It is easy to see from both graphs that an increase in *p* and *g* values result in a decrease in the frequencies of the BD-FGNBs. It is also clear from these graphs that the decrease in frequencies is more substantial with changes in *g* compared to *p*. Therefore, it can be concluded that the grading index *g* has a more significant effect on the vibration of the BD-FGNB.

The influence of the nonlocal parameter (γ) and material length scale parameter (l) are shown in Figs. 14 and 15, respectively. While the frequency values of the BD-FGNB are analyzed for the first four modes, γ and l are considered at various values ranging from 0 to 2h nm. It is

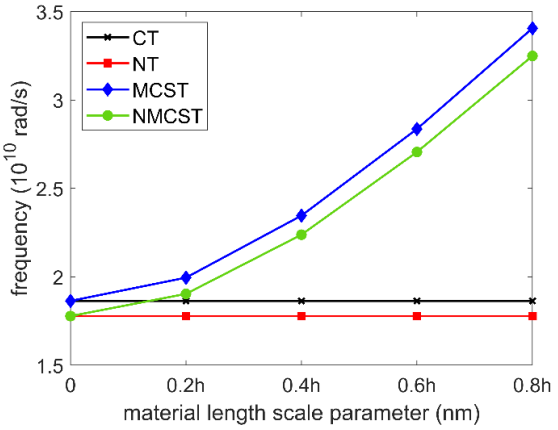

Fig. 16 Effect of l on theories

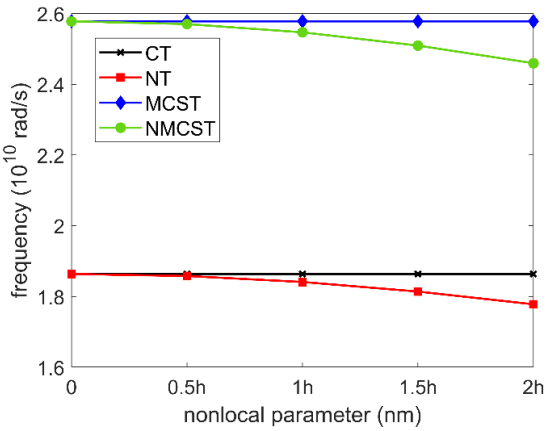

Fig. 17 Effect of γ on theories

easy to see from both graphs that these parameters affect the frequencies of the BD-FGNBs inversely. An increase in γ results in a decrease in the frequencies of the BD-FGNB, while an increase in l leads to an increment in the frequencies of the FGNB. Additionally, the graphs show that these parameters have a larger effect in higher modes.

In Fig. 16, the effects of l on different theories (CT, NT, MCST and NMCST) are analyzed. It can be seen that varying l from 0 to 2h nm increases the frequencies for MCST and NMCST, while it does not affect the frequencies of CT and NT. This is due to the fact that CT is independent of the size effect. Additionally, the reason why NT is not affected is that it does not analyze the size effect with l.

Finally, Fig. 17 shows the effects of γ on the different theories (CT, NT, MCST and NMCST). It can be seen that varying γ from 0 to 2h nm decreases the frequencies for NT and NMCST, while it does not affect the frequencies of CT and MCST. This is because, as mentioned earlier, CT is independent of the size effect, whereas MCST has no nonlocal parameter in its formulations

9. Conclusions

In this study, the vibration analysis of a nanobeam supported by deformable springs at both ends is investigated using a semi-analytical and machine learning methods. Three machine learning models including extreme gradient boosting (XGB), artificial neural network (ANN) and decision tree regression (DTR) are implemented to predict the natural frequencies of a nanobeam for the first three vibration modes. A dataset is generated that includes the material grading indices along the width and height directions, nanobeam length, material length scale parameter, and nonlocal parameter as input features. The corresponding outputs are obtained from the semi-analytical solution. The machine learning models are trained on the generated dataset and their performances are evaluated using various metrics such as R2, MAE, MAPE, RMSE and A20-index and various visualizations. The research yielded the following key conclusions,

• Machine learning models have proven to be highly effective in studying the vibration behavior of BD-FGNB. They can deliver accurate and fast predictions of natural frequencies when trained properly on a sufficient amount of dataset.

• However, relying on a single machine learning model is not sufficient for studying the vibration behavior of nanobeams. Multiple models should be trained, and their performances compared to obtain the best model with highest accuracy. This approach allows for a more thorough evaluation and helps detect any overfitting issues.

• Among the models tested, the ANN model consistently outperformed XGB and DTR across all performance metrics. XGB and DTR exhibited slight overfitting as they performed well on training dataset compared to the testing dataset. This was further validated by results from scatter plots, radar plots, and Taylor diagrams. These plots highlighted the robustness and superior performance of the ANN model.

• There are two different scale parameters (γ and l) in this theory that can examine both nonlocal and modified couple stress effects. It is observed that the parameter γ reduces the frequencies of BD-FGNB, while the parameter l increases them.

• BD-FGNBs are characterized by two distinct grading indexes (g and p), which influence the material properties along the width and height directions, respectively. An increase in the value of both grading indexes results in a decrease in the vibration frequencies of the BD-FGNB. The reason for this decrease is related to the increase in metallic properties.

References

Abouelregal, A.E. (2024), "Effect of non-local modified couple stress theory on the responses of axially moving thermoelastic nano-beams", *ZAMM Zeitschrift fur Angew. Math. und Mech.*, **104**(4), e202200233. https://doi.org/10.1002/zamm.202200233.

Agatonovic-Kustrin, S. and Beresford, R. (2000), "Basic concepts of artificial neural network (ANN) modeling and its application in pharmaceutical research", *J. Pharm. Biomed. Anal.*, **22**(5), 717-727. https://doi.org/10.1016/S0731-7085(99)00272-1.

Akgöz, B. and Civalek, Ö. (2013), "Buckling analysis of functionally graded microbeams based on the strain gradient theory", *Acta Mech.*, **224**(9), 2185-2201. https://doi.org/10.1007/S00707-013-0883-5/METRICS.

Akshaya, S.L., Prakash, A. and Bharati Raj, J. (2021), "Applications of functionally graded materials in structural engineering—A review", *Lect. Notes Civ. Eng.*, **97**, 553-566. https://doi.org/https://doi.org/10.1007/978-3-030-55115-5_51.

Al-shujairi, M. and Mollamahmutoğlu, Ç. (2018), "Dynamic stability of sandwich functionally graded micro-beam based on the nonlocal strain gradient theory with thermal effect", *Compos. Struct.*, **201**, 1018-1030. https://doi.org/10.1016/J.COMPSTRUCT.2018.06.035.

Ansari, R., Faghih Shojaei, M., Mohammadi, V., Gholami, R. and Darabi, M.A. (2014), "Nonlinear vibrations of functionally graded Mindlin microplates based on the modified couple stress theory", *Compos. Struct.*, **114**(1), 124-134. https://doi.org/10.1016/J.COMPSTRUCT.2014.04.013.

Ansari, R., Gholami, R., Faghih Shojaei, M., Mohammadi, V. and Sahmani, S. (2013), "Size-dependent bending, buckling and free vibration of functionally graded Timoshenko microbeams based on the most general strain gradient theory", *Compos. Struct.*, **100**, 385-397. https://doi.org/10.1016/J.COMPSTRUCT.2012.12.048.

Attar, F., Khordad, R., Zarifi, A. and Modabberasl, A. (2021), "Application of nonlocal modified couple stress to study of functionally graded piezoelectric plates", *Phys. B Condens. Matter*, **600**, 412623. https://doi.org/10.1016/j.physb.2020.412623.

Aziz, S.B., Abdullah, O.G. and Rasheed, M.A. (2017), "A novel polymer composite with a small optical band gap: New approaches for photonics and optoelectronics", *J. Appl. Polym. Sci.*, **134**(21), 44847. https://doi.org/10.1002/APP.44847.

Bohidar, S.K., Sharma, R. and Mishra, P.R. (2014), "Functionally graded materials: A critical review", *Int. J. Res.*, **1**(7), 289-301.

Chen, C.S., Chen, C.W. and Chen, W.R. (2013), "Dynamic stability characteristics of functionally graded plates under arbitrary periodic loads", *Int. J. Struct. Stab. Dyn.*, **13**(6). https://doi.org/10.1142/S0219455413500260.

Chen, T. and Guestrin, C. (2016), "XGBoost: A scalable tree boosting system", *Proceedings of the 22nd Acm Sigkdd International Conference on Knowledge Discovery and Data Mining*, **13-17**, 785-794. https://doi.org/https://doi.org/10.1145/2939672.293978.

Chen, X. (2024), "Vibration behavior prediction of submerged nanobeams with axially traveling supports: Numerical, analytical, and machine learning approaches", *Mech. Based Des. Struct.*, 1-31. https://doi.org/10.1080/15397734.2024.2354530.

Cheng, X., Al-Khafaji, S.H., Hashemian, M., Ahmed, M., Eftekhari, S.A., Alanssari, A.I., diaa, N.M., Karim, M.M., Toghraie, D. and Alawadi, A.H. (2023), "Statistical analysis and Neural Network Modeling of functionally graded porous nanobeams vibration in an elastic medium by considering the surface effects", *Eng. Appl. Artif. Intell.*, **123**, 106313. https://doi.org/10.1016/J.ENGAPPAI.2023.106313.

Civalek, Ö., Uzun, B. and Yaylı, M.Ö. (2023), "Size-dependent nonlinear stability response of perforated nano/microbeams via Fourier series", *Arch. Appl. Mech.*, **93**(12), 4425-4443. https://doi.org/10.1007/s00419-023-02501-5.

Cosserat, E.M.P. and Cosserat, F. (1909), *Théorie des Corps Déformables*, A. Hermann et fils.

Cui, L., Kiernan, S. and Gilchrist, M.D. (2009), "Designing the energy absorption capacity of functionally graded foam materials", *Mater. Sci. Eng. A*, **507**(1-2), 215-225. https://doi.org/10.1016/J.MSEA.2008.12.011.

Demšar, J. (2006), "Statistical comparisons of classifiers over multiple data sets", *J. Mach. Learn. Res.*, **7**, 1-30

Ebrahimi, F. and Barati, M.R. (2018), "A modified nonlocal couple stress-based beam model for vibration analysis of higher- order FG nanobeams", *Mech. Adv. Mater. Struct.*, **25**(13), 1121-1132. https://doi.org/10.1080/15376494.2017.1365979.

Eringen, A.C. (1977), "Screw dislocation in non-local elasticity", *J. Phys. D. Appl. Phys.*, **10**(5), 671. https://doi.org/10.1088/0022-3727/10/5/009.

Esen, I., Abdelrahman, A.A. and Eltaher, M.A. (2021), "On vibration of sigmoid/symmetric functionally graded nonlocal strain gradient nanobeams under moving load", *Int. J. Mech. Mater. Des.*, **17**(3), 721-742. https://doi.org/10.1007/s10999-021-09555-9.

Eshkofti, K. and Hosseini, S.M. (2023), "A gradient-enhanced physics-informed neural network (gPINN) scheme for the coupled non-fickian/non-fourierian diffusion-thermoelasticity analysis: A novel gPINN structure", *Eng. Appl. Artif. Intell.*, **126**, 106908. https://doi.org/10.1016/j.engappai.2023.106908

Eshkofti, K. and Hosseini, S.M. (2024a), "The modified physics-informed neural network (PINN) method for the thermoelastic wave propagation analysis based on the Moore-Gibson-Thompson theory in porous materials", *Compos. Struct.*, **348**, 118485. https://doi.org/10.1016/j.compstruct.2024.118485

Eshkofti, K. and Hosseini, S.M. (2024b), "A new modified deep learning technique based on physics-informed neural networks (PINNs) for the shock-induced coupled thermoelasticity analysis in a porous material", *J. Therm. Stress.*, **47**(6), 798-825. https://doi.org/10.1080/01495739.2024.2321205

Fleck, N.A. and Hutchinson, J.W. (1993), "A phenomenological theory for strain gradient effects in plasticity", *J. Mech. Phys. Solids*, **41**(12), 1825-1857. https://doi.org/10.1016/0022-5096(93)90072-N.

Fleck, N.A. and Hutchinson, J.W. (1997), "Strain gradient plasticity", *Adv. Appl. Mech.*, 295-361. https://doi.org/10.1016/S0065-2156(08)70388-0.

Fleck, N.A. and Hutchinson, J.W. (2001), "A reformulation of strain gradient plasticity", *J. Mech. Phys. Solids*, **49**(10), 2245-2271. https://doi.org/10.1016/S0022-5096(01)00049-7.

Friedman, J., Hastie, T. and Tibshirani, R. (2000), "Additive logistic regression: A statistical view of boosting (With discussion and a rejoinder by the authors)", *Annals Statistics* **28**(2), 337-407. https://doi.org/10.1214/AOS/1016218223.

Gao, Y., Xiao, W.S. and Zhu, H. (2019), "Nonlinear vibration of functionally graded nano-tubes using nonlocal strain gradient theory and a two-steps perturbation method", *Struct. Eng. Mech.*, **69**(2), 205-219. https://doi.org/10.12989/sem.2019.69.2.205.

Ghadiri, M. and Shafiei, N. (2016), "Vibration analysis of rotating functionally graded Timoshenko microbeam based on modified couple stress theory under different temperature distributions", *Acta Astronaut.*, **121**, 221-240. https://doi.org/10.1016/J.ACTAASTRO.2016.01.003.

Ghandourah, E.E., Ahmed, H.M., Eltaher, M.A., Attia, M.A. and Abdraboh, A.M. (2021), "Free vibration of porous FG nonlocal modified couple nanobeams via a modified porosity model", *Adv. Nano Res.*, **11**(4), 405-422. https://doi.org/10.12989/anr.2021.11.4.405.

Hao-nan, L., Cheng, L., Ji-ping, S. and Lin-quan, Y. (2021), "Vibration analysis of rotating functionally graded piezoelectric nanobeams based on the nonlocal elasticity theory", *J. Vib. Eng. Technol.*, **9**(6), 1155-1173. https://doi.org/10.1007/s42417-021-00288-9.

Hasan, M.N., Salman, M.S., Islam, A., Znad, H. and Hasan, M.M. (2021), "Sustainable composite sensor material for optical cadmium(II) monitoring and capturing from wastewater", *Microchem. J.*, **161**, 105800. https://doi.org/10.1016/J.MICROC.2020.105800.

Hassaine, N., Touat, N., Dahak, M., Fellah, A. and Saimi, A. (2024), "Study of crack's effect on the natural frequencies of bi-directional functionally graded beam", *Mech. Based Des. Struct.*, **52**(1), 375-385.

https://doi.org/10.1080/15397734.2022.2113408.
Heidary, Z., Ramezani, S.R. and Mojra, A. (2023), "Exploring the benefits of functionally graded carbon nanotubes (FG-CNTs) as a platform for targeted drug delivery systems", *Comput. Methods Programs Biomed.*, **238**, 107603. https://doi.org/10.1016/J.CMPB.2023.107603.
Hosseini-Hashemi, S., Bedroud, M. and Nazemnezhad, R. (2013), "An exact analytical solution for free vibration of functionally graded circular/annular Mindlin nanoplates via nonlocal elasticity", *Compos. Struct.*, **103**, 108-118. https://doi.org/10.1016/J.COMPSTRUCT.2013.02.022.
Hosseini, S.A.H. and Rahmani, O. (2016), "Thermomechanical vibration of curved functionally graded nanobeam based on nonlocal elasticity", *J. Therm. Stress.*, **39**(10), 1252-1267. https://doi.org/10.1080/01495739.2016.1215731.
Jung, W.Y. and Han, S.C. (2013), "Analysis of Sigmoid Functionally Graded Material (S-FGM) Nanoscale Plates Using the Nonlocal Elasticity Theory", *Math. Probl. Eng.*, **2013**(1), 476131. https://doi.org/10.1155/2013/476131.
Karamanli, A. and Vo, T.P. (2020), "Size-dependent behaviour of functionally graded sandwich microbeams based on the modified strain gradient theory", *Compos. Struct.*, **246**, 112401. https://doi.org/10.1016/J.COMPSTRUCT.2020.112401.
Karamanli, A. and Vo, T.P. (2021), "A quasi-3D theory for functionally graded porous microbeams based on the modified strain gradient theory", *Compos. Struct.*, **257**, 113066. https://doi.org/10.1016/J.COMPSTRUCT.2020.113066.
Ke, L.L. and Wang, Y.S. (2011), "Size effect on dynamic stability of functionally graded microbeams based on a modified couple stress theory", *Compos. Struct.*, **93**(2), 342-350. https://doi.org/10.1016/J.COMPSTRUCT.2010.09.008.
Koiter, W.T. (1969), *Couple-Stresses in the Theory of Elasticity, I & II*. https://sid.ir/paper/605637/en.
Lal, R. and Dangi, C. (2019), "Thermomechanical vibration of bi-directional functionally graded non-uniform timoshenko nanobeam using nonlocal elasticity theory", *Compos. Part B Eng.*, **172**, 724-742. https://doi.org/10.1016/J.COMPOSITESB.2019.05.076.
Lam, D.C.C., Yang, F., Chong, A.C.M., Wang, J. and Tong, P. (2003), "Experiments and theory in strain gradient elasticity", *J. Mech. Phys. Solids*, **51**(8), 1477-1508. https://doi.org/10.1016/S0022-5096(03)00053-X.
Le, T.T. (2021), "Prediction of tensile strength of polymer carbon nanotube composites using practical machine learning method", *J. Compos. Mater.*, **55**(6), 787-811. https://doi.org/10.1177/0021998320953540.
Li, C., Wang, P.Y., Luo, Q.Y. and Li, S. (2021), "Free vibration of axially moving functionally graded nanoplates based on the nonlocal strain gradient theory", *Int. J. Acoust. Vib.*, **25**(4), 587-596. https://doi.org/10.20855/ijav.2020.25.41725.
Li, L. and Hu, Y. (2017), "Torsional vibration of bi-directional functionally graded nanotubes based on nonlocal elasticity theory", *Compos. Struct.*, **172**, 242-250. https://doi.org/10.1016/J.COMPSTRUCT.2017.03.097.
Li, X., Li, L., Hu, Y., Ding, Z. and Deng, W. (2017), "Bending, buckling and vibration of axially functionally graded beams based on nonlocal strain gradient theory", *Compos. Struct.*, **165**, 250-265. https://doi.org/10.1016/J.COMPSTRUCT.2017.01.032.
Lou, J., He, L. and Du, J. (2015), "A unified higher order plate theory for functionally graded microplates based on the modified couple stress theory", *Compos. Struct.*, **133**, 1036-1047. https://doi.org/10.1016/J.COMPSTRUCT.2015.08.009.
Ma, H.M., Gao, X.L. and Reddy, J.N. (2008), "A microstructure-dependent Timoshenko beam model based on a modified couple stress theory", *J. Mech. Phys. Solids*, **56**(12), 3379-3391. https://doi.org/10.1016/J.JMPS.2008.09.007.
Mindlin, R.D. and Tiersten, H.F. (1962), "Effects of couple-stresses in linear elasticity", *Arch. Ration. Mech. Anal.*, **11**(1), 415-448. https://doi.org/10.1007/BF00253946.
Mollamahmutoğlu, Ç. and Mercan, A. (2019), "A novel functional and mixed finite element analysis of functionally graded micro-beams based on modified couple stress theory", *Compos. Struct.*, **223**, 110950. https://doi.org/10.1016/J.COMPSTRUCT.2019.110950.
Müller, E., Drašar, Č., Schilz, J. and Kaysser, W.A. (2003), "Functionally graded materials for sensor and energy applications", *Mater. Sci. Eng. A*, **362**(1-2), 17-39. https://doi.org/10.1016/S0921-5093(03)00581-1.
Nejad, M.Z., Hadi, A. and Rastgoo, A. (2016), "Buckling analysis of arbitrary two-directional functionally graded Euler-Bernoulli nano-beams based on nonlocal elasticity theory", *Int. J. Eng. Sci.*, **103**, 1-10. https://doi.org/10.1016/J.IJENGSCI.2016.03.001.
Nguyen, H.X., Atroshchenko, E., Ngo, T., Nguyen-Xuan, H. and Vo, T.P. (2019), "Vibration of cracked functionally graded microplates by the strain gradient theory and extended isogeometric analysis", *Eng. Struct.*, **187**, 251-266. https://doi.org/10.1016/J.ENGSTRUCT.2019.02.032.
Nguyen, H.X., Atroshchenko, E., Nguyen-Xuan, H. and Vo, T.P. (2017a), "Geometrically nonlinear isogeometric analysis of functionally graded microplates with the modified couple stress theory", *Comput. Struct.*, **193**, 110-127. https://doi.org/10.1016/J.COMPSTRUC.2017.07.017.
Nguyen, H.X., Nguyen, T.N., Abdel-Wahab, M., Bordas, S.P.A., Nguyen-Xuan, H. and Vo, T.P. (2017b), "A refined quasi-3D isogeometric analysis for functionally graded microplates based on the modified couple stress theory", *Comput. Methods Appl. Mech. Eng.*, **313**, 904-940. https://doi.org/10.1016/J.CMA.2016.10.002.
Park, S.K. and Gao, X.L. (2006), "Bernoulli-Euler beam model based on a modified couple stress theory", *J. Micromech. Microeng.*, **16**(11), 2355-2359. https://doi.org/10.1088/0960-1317/16/11/015.
Pham, Q.H., Nguyen, P.C., Tran, V.K., Lieu, Q.X. and Tran, T.T. (2023), "Modified nonlocal couple stress isogeometric approach for bending and free vibration analysis of functionally graded nanoplates", *Eng. Comput.*, **39**(1), 993-1018. https://doi.org/10.1007/s00366-022-01726-2.
Pham, Q.H., Tran, V.K., Tran, T.T., Nguyen, P.C. and Malekzadeh, P. (2022), "Dynamic instability of magnetically embedded functionally graded porous nanobeams using the strain gradient theory", *Alexandria Eng. J.*, **61**(12), 10025-10044. https://doi.org/10.1016/J.AEJ.2022.03.007.
Pirmoradian, M., Torkan, E., Zali, H., Hashemian, M. and Toghraie, D. (2020), "Statistical and parametric instability analysis for delivery of nanoparticles through embedded DWCNT", *Phys. A Stat. Mech. its Appl.*, **554**, 123911. https://doi.org/10.1016/J.PHYSA.2019.123911.
Rahaeifard, M., Kahrobaiyan, M.H., Ahmadian, M.T. and Firoozbakhsh, K. (2013), "Strain gradient formulation of functionally graded nonlinear beams", *Int. J. Eng. Sci.*, **65**, 49-63. https://doi.org/10.1016/J.IJENGSCI.2013.02.002.
Rao, Y. and Wong, C.P. (2004), "Material characterization of a high-dielectric-constant polymer-ceramic composite for embedded capacitor for RF applications", *J. Appl. Polym. Sci.*, **92**(4), 2228-2231. https://doi.org/10.1002/APP.13690.
Rao, Y., Yue, J. and Wong, C.P. (2001), "High K polymer-ceramic nano-composite development, characterization, and modeling for embedded capacitor RF application", *2001 Proceedings of the 51st Electronic Components and Technology Conference* (Cat. No. 01CH37220) (pp. 1408-1412). https://doi.org/10.1109/ECTC.2001.928018.
Renardy, M., Joslyn, L.R., Millar, J.A. and Kirschner, D.E. (2021), "To Sobol or not to Sobol? The effects of sampling schemes in

systems biology applications", *Math. Biosci.*, **337**, 108593. https://doi.org/10.1016/J.MBS.2021.108593.

Shen, J.P., Wang, P.Y., Gan, W.T. and Li, C. (2020), "Stability of Vibrating Functionally Graded Nanoplates with Axial Motion Based on the Nonlocal Strain Gradient Theory", *Int. J. Struct. Stab. Dyn.*, **20**(8). https://doi.org/10.1142/S0219455420500881.

Shishesaz, M., Hosseini, M., Naderan Tahan, K. and Hadi, A. (2017), "Analysis of functionally graded nanodisks under thermoelastic loading based on the strain gradient theory", *Acta Mech.*, **228**(12), 4141-4168. https://doi.org/10.1007/S00707-017-1939-8/METRICS.

Şimşek, M., Kocatürk, T. and Akbaş, Ş.D. (2013), "Static bending of a functionally graded microscale Timoshenko beam based on the modified couple stress theory", *Compos. Struct.*, **95**, 740-747. https://doi.org/10.1016/J.COMPSTRUCT.2012.08.036.

Şimşek, M. and Reddy, J.N. (2013a), "Bending and vibration of functionally graded microbeams using a new higher order beam theory and the modified couple stress theory", *Int. J. Eng. Sci.*, **64**, 37-53. https://doi.org/10.1016/J.IJENGSCI.2012.12.002.

Şimşek, M. and Reddy, J.N. (2013b), "A unified higher order beam theory for buckling of a functionally graded microbeam embedded in elastic medium using modified couple stress theory", *Compos. Struct.*, **101**, 47-58. https://doi.org/10.1016/J.COMPSTRUCT.2013.01.017.

Tariq, A., Abualshar, B., Deliktas, B., Song, C.R., Al-Nimri, B., Barret, B., Silvey, A. and Glennie, N. (2024a), "ANN-based evaluation system for erosion resistant highway shoulder rocks", *Int. J. Geo-Eng.*, **15**(1), 1-18. https://doi.org/10.1186/s40703-024-00216-2.

Tariq, A., Uzun, B., Deliktaş, B. and Yayli, M.Ö. (2024b), "A machine learning approach for buckling analysis of a bi-directional FG microbeam", *Microsyst. Technol.*, 1-22. https://doi.org/10.1007/s00542-024-05724-w.

Tariq, A., Uzun, B., Deliktaş, B. and Yaylı, M.Ö. (2024c), "Assessment of machine learning methods predicting the axial vibration frequencies of microbars", *ZAMM J. Appl. Math. Mech.*, **104**(3), e202300916. https://doi.org/10.1002/ZAMM.202300916.

Tariq, A., Uzun, B., Deliktaş, B. and Yaylı, M.Ö. (2024d), "An investigation on ensemble machine learning algorithms for nonlinear stability response of a two-dimensional FG nanobeam", *J. Brazil. Soc. Mech. Sci. Eng.*, **46**(9), 1-24. https://doi.org/10.1007/s40430-024-05093-5.

Tariq, A., Uzun, B., Deliktaş, B., Yaylı, M.Ö., Us¸raus¸ra Uzun, B., Deliktas¸, D. and Ozg€ Ur Yaylı, M.€. (2024e), "Vibration analysis of embedded porous nanobeams under thermal effects using boosting machine learning algorithms and semi-analytical approach", *Mech. Adv. Mater. Struct.*, 1-24. https://doi.org/10.1080/15376494.2024.2320809.

Thai, S., Thai, H.T., Vo, T.P. and Nguyen-Xuan, H. (2017), "Nonlinear static and transient isogeometric analysis of functionally graded microplates based on the modified strain gradient theory", *Eng. Struct.*, **153**, 598-612. https://doi.org/10.1016/J.ENGSTRUCT.2017.10.002.

Toupin, R.A. (1962), "Elastic materials with couple-stresses", *Arch. Ration. Mech. Anal.*, **11**(1). https://hal.science/hal-00852443.

Tran, V.T., Nguyen, T.K., Nguyen-Xuan, H. and Abdel Wahab, M. (2023), "Vibration and buckling optimization of functionally graded porous microplates using BCMO-ANN algorithm", *Thin Wall. Struct.*, **182**, 110267. https://doi.org/10.1016/J.TWS.2022.110267.

Uymaz, B. (2013), "Forced vibration analysis of functionally graded beams using nonlocal elasticity", *Compos. Struct.*, **105**, 227-239. https://doi.org/10.1016/J.COMPSTRUCT.2013.05.006.

Voigt, W. (1887), *Theoretische Studien Über Die Elasticitätsverhältnisse Der Krystalle*, Königliche Gesellschaft der Wissenschaften zu Göttingen.

Watari, F., Yokoyama, A., Omori, M., Hirai, T., Kondo, H., Uo, M. and Kawasaki, T. (2004), "Biocompatibility of materials and development to functionally graded implant for bio-medical application", *Compos. Sci. Technol.*, **64**(6), 893-908. https://doi.org/10.1016/J.COMPSCITECH.2003.09.005.

Xu, M., Watanachaturaporn, P., Varshney, P.K. and Arora, M.K. (2005), "Decision tree regression for soft classification of remote sensing data", *Remote Sens. Environ.*, **97**(3), 322-336. https://doi.org/10.1016/J.RSE.2005.05.008.

Yan, C.A., Vescovini, R. and Fantuzzi, N. (2023), "A neural network-based approach for bending analysis of strain gradient nanoplates", *Eng. Anal. Bound. Elem.*, **146**, 517-530. https://doi.org/10.1016/J.ENGANABOUND.2022.10.017.

Yang, F., Chong, A.C.M., Lam, D.C.C. and Tong, P. (2002), "Couple stress based strain gradient theory for elasticity", *Int. J. Solids Struct.*, **39**(10), 2731-2743. https://doi.org/10.1016/S0020-7683(02)00152-X.

Yu, X.L. and Zhou, X.P. (2024), "A nonlocal energy-informed neural network for peridynamic correspondence material models", *Eng. Anal. Bound. Elem.*, **160**, 273-297.

Zargaripoor, A., Daneshmehr, A., Isaac Hosseini, I. and Rajabpoor, A. (2018), "Free vibration analysis of nanoplates made of functionally graded materials based on nonlocal elasticity theory using finite element method", *J. Comput. Appl. Mech.*, **49**(1), 86-101. https://doi.org/10.22059/JCAMECH.2018.248906.223.

Zheng, Y. fang, Zhou, Y., Wang, F. and Chen, C. ping. (2024), "Nonlinear deformation analysis of magneto-electro-elastic nanobeams resting on elastic foundation by using nonlocal modified couple stress theory", *Eur. J. Mech. A/Solids*, **103**, 105158. https://doi.org/10.1016/j.euromechsol.2023.105158.

Zyoud, S.H., Almoadi, A., AlAbdulaal, T.H., Alqahtani, M.S., Harraz, F.A., Al-Assiri, M.S., Yahia, I.S., Zahran, H.Y., Mohammed, M.I. and Abdel-wahab, M.S. (2023), "Structural, optical, and electrical investigations of Nd2O3-Doped PVA/PVP polymeric composites for electronic and optoelectronic applications", *Polym.*, **15**(6), 1351. https://doi.org/10.3390/POLYM15061351.

Zhou, X.P. and Yu, X.L. (2024), "Transfer learning enhanced nonlocal energy-informed neural network for quasi-static fracture in rock-like materials", *Comput. Meth. Appl. Mech. Eng.*, **430**, 117226.

CC

Appendix

The matrix components are as follows:

$$\Omega_{11} = -S_0 - \frac{[\rho A]_{eff}\gamma^2\omega^2}{L} + \frac{\omega^2[\rho I]_{eff}}{L} + \sum_{j=1}^{\infty} \frac{2L\omega^2[\rho A]_{eff}(\vartheta_3 - L^2\gamma^2\omega^2[\rho A]_{eff} + \vartheta_1)}{\vartheta_3 j^2\pi^2 + L^2\vartheta_2 + j^2\vartheta_1} \quad \text{(A1)}$$

$$\Omega_{12} = \frac{[\rho A]_{eff}\gamma^2\omega^2}{L} - \frac{\omega^2[\rho I]_{eff}}{L} - \sum_{j=1}^{\infty} \frac{2(-1)^j L\omega^2[\rho A]_{eff}(\vartheta_3 - L^2\gamma^2\omega^2[\rho A]_{eff} + \vartheta_1)}{\vartheta_3 j^2\pi^2 + L^2\vartheta_2 + j^2\vartheta_1} \quad \text{(A2)}$$

$$\Omega_{21} = \frac{[\rho A]_{eff}\gamma^2\omega^2}{L} - \frac{\omega^2[\rho I]_{eff}}{L} - \sum_{j=1}^{\infty} \frac{2(-1)^j L\omega^2[\rho A]_{eff}(\vartheta_3 - L^2\gamma^2\omega^2[\rho A]_{eff} + \vartheta_1)}{\vartheta_3 j^2\pi^2 + L^2\vartheta_2 + j^2\vartheta_1[\rho I]_{eff}} \quad \text{(A3)}$$

$$\Omega_{22} = -S_L - \frac{[\rho A]_{eff}\gamma^2\omega^2}{L} + \frac{\omega^2[\rho I]_{eff}}{L} + \sum_{j=1}^{\infty} \frac{2L\omega^2[\rho A]_{eff}(\vartheta_3 - L^2\gamma^2\omega^2[\rho A]_{eff} + \vartheta_1)}{\vartheta_3 j^2\pi^2 + L^2\vartheta_2 + j^2\vartheta_1} \quad \text{(A4)}$$